Short Papers

A Contribution to the Modeling of Longitudinally Periodic Waveguides by the Help of the TLM Method

Marc Walter, Oliver Pertz, and Adalbert Beyer

***Abstract*—To efficiently simulate longitudinally periodic waveguide, the Floquet's theorem is implemented to modify the transmission-line matrix (TLM) algorithm. In the literature, similar algorithms are presented for the finite-difference time-domain method and fundamental problems are addressed. The aim of this paper is to explain and solve these problems and misunderstandings and to extend the approach to the TLM method. Simulation results show the validity of the technique proposed.**

***Index Terms*—Capacitive loaded rectangular waveguide, coupling factors, f-β diagram, Floquet's theorem, periodic waveguide structures.**

I. Introduction

In [1] and [2], the possibility of simulating longitudinally periodic structures using the finite-difference time-domain (FDTD) method is described. Besides the algorithm for two FDTD networks there are also coupling factors shown which allow a simulation with only one network. It is mentioned in this contribution that the same concept is applicable to the transmission-line matrix (TLM) method, but there are no further statements given for this. Differences between the TLM method and the FDTD method exist among other things in the different arrangement of the field components, whereby even coupling factors can differ. Further considerations have been made to check this question.

II. Theory and Algorithms for the Simulation of Periodic Waveguide Structures

As mentioned in Section I, the problem addressed above firstly represents a general task. The mathematical background is not trivial at all. Thus, some mathematical basics of Floquet's theorem are represented [3]. It can be shown that a vector differential equation system of the form

$$\dot{\mathbf{x}} = \mathbf{A}(t)\mathbf{x} \tag{1}$$

with the column vector $\mathbf{x}$ and the T periodic $n \times n$ matrix $\mathbf{A}(t)$, is given by functions $\mathbf{x}(t)$, which have the property

$$\mathbf{x}(t+T) = e^{\gamma T}\mathbf{x}(t) \tag{2}$$

with a constant $T > 0$ and a complex quantity γ representing the eigenvalue as solution, whereby γ is uniquely determined up to an additive term $jm(2\pi/T)$, m integer. It can be shown that $\mathbf{x}(t)$ can also be written in the form

$$\mathbf{x}(t) = e^{\gamma t}\mathbf{f}(t) \quad \text{with } \mathbf{f}(t+T) = \mathbf{f}(t). \tag{3}$$

This is the general form of the Floquet's theorem. In the literature, the calculation of periodic waveguides is usually performed by the help of the theorem given in (3).

Manuscript received January 30, 1998.

The authors are with the Department of Electrical Engineering, Gerhard-Mercator-University Duisburg, D-47057 Duisburg, Germany (e-mail: a.beyer@uni-duisburg.de).

Publisher Item Identifier S 0018-9480(00)07399-3.

Now, applying the Floquet's theorem to longitudinally periodic waveguides with z_1 and z_2 two cross-sectional planes of which distance $l = z_2 - z_1$ matches with the physical period of the waveguide $F(z) = e^{\pm\gamma z}\Phi(z)$ with $\Phi(z+l) = \Phi(z)$ and $F(z) \in \{E_x, E_y, E_z, H_x, H_y, H_z\}$ is valid. This yields

$$F(z+l) = e^{\pm\gamma l}F(z). \tag{4}$$

Generally, even for periodic waveguides with lossless materials, it can be assumed that the real part of the complex propagation coefficient $\gamma = \alpha + j\beta$ does not vanish. Following the Floquet's theorem [see (4)] the possible values for γ are uniquely determined, up to an additive term $jm(2\pi/T)$, m integer. Thus, for a given phase constant β even the attenuation constant α is uniquely determined. Usually, the correlation of α and β is not known so that even by simulating periodic waveguides with lossless materials the approximation $\alpha = 0$ has to be used. Attenuation would, hence, become noticeable by a temporal reduction of the field energy similar to the case of a simulation of longitudinally homogeneous lines. The approximation can be regarded as valid if the attenuation is not too large.

Although the z dependency of the field components is not really harmonic, the relationship between z_1 and z_2 corresponds to the case of longitudinally homogeneous waveguides if $\alpha = 0$ is assumed. Hence, the same exchange algorithm can be used which has already been described for longitudinally homogeneous lines. This is, however, only under the assumption of a complex-valued TLM network for the simulation valid.

A simulation of standing waves permits a field component to be separated in the form $F(z,t) = F\cos(\beta z)F_t(t)$. Then, between two arbitrary planes z_1 and z_2 the relations $F(z_1,t) = v_2F(z_2,t), F(z_2,t) = v_1F(z_1,t)$, with

$$v_1 = \frac{1}{v_2} = \frac{\cos(\beta(z_1+l))}{\cos(\beta z_1)} \tag{5}$$

$l = z_2 - z_1 > 0$ are valid. The factor v_1 in (5) corresponds to the operator given in [1]. Hence, it seems to be sufficient to use equations of the form $U_2^i(z_1) = v_2U_9^r(z_2), U_9^i(z_2) = v_1U_2^r(z_1)$ (analogously for the ports 4 and 8 of the symmetrical condensed node (SCN) in Fig. 1) for a new exchange algorithm, whereby only a real-valued TLM network is then needed. It is, however, easy to show that this is not sufficient. To prove the last statement the idea is the following. Let

$$\cos(\xi + \Delta\xi) = v_1\cos(\xi) \tag{6}$$

with given factor v_1. Hereby, the following conditions are valid: $\xi = z_1$ and $\Delta\xi = \beta l$. Let first $|v_1| \leq 1$, then $\Delta\xi$ can be determined as

$$\Delta\xi = \arccos(v_1\cos(\xi)) - \xi. \tag{7}$$

Because of $|v_1| \leq 1$ different values of $\Delta\xi$ can be calculated for different values of ξ from this equation. The expression $\Delta\xi$ should be independent from ξ because of having prescribed that $\Delta\xi = \beta l$. Coordinates like ξ cannot be included into TLM simulations because of those working exclusively coordinate free. Otherwise, ξ is unknown, the phase constant $\beta = \Delta\xi/l$ is also unknown for given l.

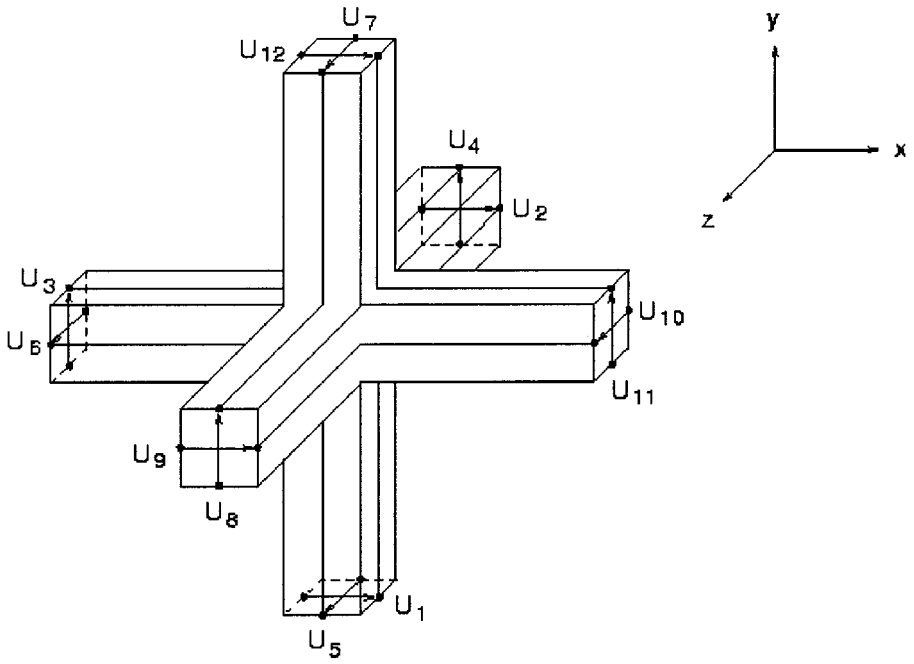

Fig. 1. Symbolic representation of the SCN [6].

At this point it can also be argued in opposition that the factor v_1 does not uniquely determine the phase constant β if the value for $\xi = z_1$ is not even known. In other words, the zero phase would have to be known if all z dependencies are expressed relatively to z_1 and with it corresponding to the zero phase βz_1. Otherwise, for a given value v_1, a nondenumerably infinite amount of solutions exists for β. For the coupling factors, however, only a countably infinite amount of possibilities exists for β what corresponds to the statements mentioned above concerning the Floquet's theorem.

A significant simulation result cannot be expected with this real-valued network variant because of a given value v_1 being possibly associated with more or less arbitrary values of β. That way, no frequency changes could be observed after changing β in our first simulations. For $|v_1| > 1$, the same argumentation applies to v_2. Probably this is also the explanation for a statement given in [1] which claims that excitations would have to be carried out carefully in order to be "efficient" for certain zero-phase angles.

The problems can then be eliminated if the zero phase, i.e., z_1, can be fixed. This could be done simplest by the help of an electric ($\beta z_1 = \pi$) or magnetic ($\beta z_1 = 0$) wall at z_1. For the simulations, a magnetic wall was chosen. The coupling factor simplifies then to

$$v_1 = \cos(\beta l) = \frac{1}{v_2}. \tag{8}$$

The formulation of the exchange algorithm can now be described easily. As mentioned above, the magnetic wall be situated at z_1. Because of this magnetic wall it is valid in an SCN for $U_2^i(z_1)$: $U_2^i(z_1) = U_2^r(z_1)$. Hence, $U_9^r(z_2)$ is given by the scattering. Therefore, it has to be calculated in a way that $U_9(z_2) = v_1 U_2(z_1)$. Subsequently, it follows

$$U_9^i(z_2) = 2v_1 U_2^r(z_1) - U_9^r(z_2). \tag{9}$$

With this exchange algorithm for the cross-section planes at z_1 and z_2 some experiments have successfully been realized. Hereby, it was not necessary to be in particular careful while exciting. This matches also with a statement given in [1], where a magnetic wall made the algorithm "robust," too.

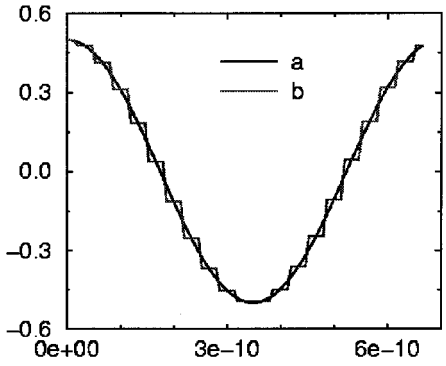

Fig. 2. Simulation of free harmonic TEM-waves in vacuum after a step from $\beta = 0\ \mathrm{m}^{-1}$ up to $\beta = 30\ \mathrm{m}^{-1}$. Curve a: one single TLM node. Curve b: 10 TLM nodes one after another in propagation direction.

III. Simulations and Evaluations

A. Peculiarities of the Algorithm

Simulations with our method are usually done by increasing the phase constant β stepwise and using the field of the previous simulation part directly as excitation field for the simulation par with the new value of β. This nonperfect excitation causes the appearance of higher frequencies.

Fig. 2 shows the simulation of two free harmonic TEM waves in vacuum after a step of the phase constant β from $0\ \mathrm{m}^{-1}$ up to $30\ \mathrm{m}^{-1}$. For curve a, only one single step in the space domain in the propagation direction was used. The behavior of the depicted field components appears very smooth. For curve b in Fig. 2, ten layers of the simulation range from curve a have been assembled to one space domain which can be thought of as a periodic structure in spite of its homogeneity. Opposite to curve a, however, a sudden appearance of not decaying

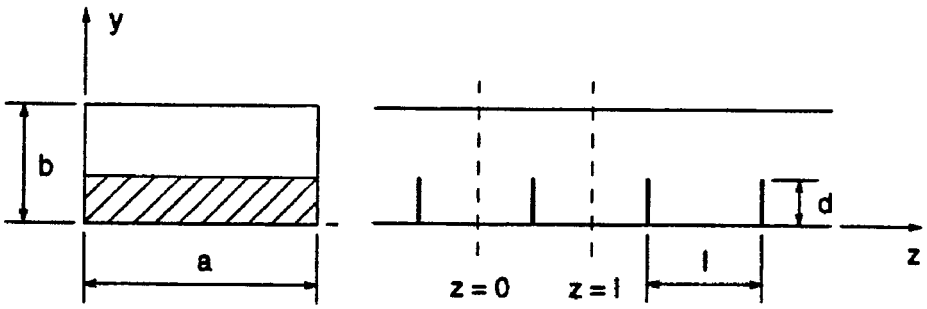

Fig. 3. Periodic and capacitively loaded ideal rectangular waveguide: $a = 20$ mm, $b = 10$ mm, $d = 3$ mm, and $l = 30$ mm.

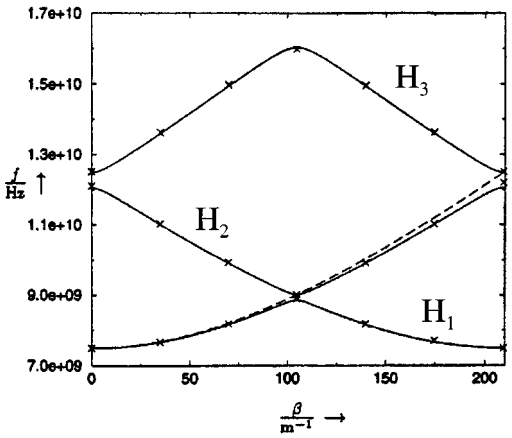

Fig. 4. f-β of a periodically capacitive loaded rectangular waveguide. Continuos line: analytical approximate calculation according to [5]. Symbols: simulation results. Dashed line: curve of the H_{10}-type of the not capacitively loaded rectangular waveguide.

high-frequency components could be observed after the phase step leading to the stepped behavior of the field component. It can be shown that these steps belong to phase constants β_n, with $\beta_n \Delta z = \beta \Delta z + n2\pi$, which lead to identical coupling factors v_1 and v_2. In [4], it is pointed out that the appearance of wavetypes at higher frequencies even cannot be suppressed using smaller steps of β. Nevertheless, this effect does not restrict the validity of the algorithm in any way.

B. Simulation of a Periodic Capacitively Loaded Rectangular Waveguide

A periodic capacitively loaded rectangular waveguide is calculated in ([5], chs. 9.5, 9.7) using two different methods. The capacitive loading leads to separated stopbands and passbands. For the structure represented in Fig. 3, the calculations have been performed for the three lowest modes (solid lines in Fig. 4). We used a value of $d = 0.3b$ to demonstrate that even very small stopbands can be resolved with our method.

The simulation result presented in Fig. 4 was calculated by the help of a Fourier transform (symbols). The weak capacitive loading leads to the small stop areas as predicted by the approximate calculations. Nevertheless, the periodicity of the capacitive loading can uniquely be recognized regarding the curves. In comparison to this, the curve of an undisturbed rectangular waveguide is also shown (dashed line).

IV. Conclusion

In the frame of this work, diverse problems have been treated in order to simulate and analyze longitudinally periodic structures efficiently using the TLM method. First of all, the mathematical basics for the treatment of periodic waveguides and the necessary algorithm for the simulation has been explained and described. The conditions of an exchange algorithm for TLM applications according to its efficiency and robustness have thereby been discussed. This treatment rendered it possible to discover and clear up some problems addressed in the literature.

In order to show the feasibility of the technique presented, a periodic capacitively loaded rectangular waveguide has successfully been simulated.

References

[1] M. Celuch-Marcysiak *et al.*, "Effective time domain analysis of periodic structures," in *Proc. 23rd European Microwave Conf.*, Madrid, Spain, Sept. 1993, pp. 293–295.

[2] M. Celuch-Marcysiak *et al.*, "Spatially looped algorithms for time-domain analysis of periodic structures," *IEEE Trans. Microwave Theory Tech.*, vol. 43, pp. 860–865, Apr. 1995.

[3] V. A. Yakubovich *et al.*, *Linear Differential Equations with Periodic Coefficients*. New York: Wiley, 1975, vol. 1.

[4] M. Walter, *Anwendung der TLM-Methode auf längsperiodische Leitungsstrukturen der Mikrowellenund Millimeterwellentechnik*. Duisburg, Germany: Gerhard Mercator Univ. Duisburg, 1996. (in German).

[5] R. E. Collin, *Field Theory of Guided Waves*, 2nd ed. Piscataway, NJ: IEEE Press, 1991.

[6] P. B. Johns, "A symmetrical condensed node for the TLM-method," *IEEE Trans. Microwave Theory Tech.*, vol. MTT-35, pp. 370–377, Apr. 1987.

Analysis of Partial-Height Ferrite-Slab Differential Phase-Shift Sections

Bernice M. Dillon and Andrew A. P. Gibson

***Abstract*—Rectangular waveguide loaded with transversely magnetized ferrite slabs is a classic arrangement used in the construction of high-power differential phase-shift circulators. The characterization of this structure is extended in this paper by using a combined magnetostatic/microwave finite-element method to evaluate propagation characteristics in terms of material parameters, frequency, and bias field. Magnetic flux density was found to vary by typically 20% across a partial-height ferrite slab. Experimental phase-shift data agreed to within 5% of numerical calculations for a 9.25-GHz device. Supplementary design data are presented for the first higher order mode in the cutoff plane, the effect of material properties on phase shift, and to compare below and above resonance operation.**

I. Introduction

The principle of operation of a ferrite circulator using a gyrator was first proposed by Hogan [1]. In rectangular waveguide, a practical implementation uses a ferrite differential phase-shift section and two 3-dB directional couplers or hybrid T-junctions [2], [3]. Differential phase shifters (DPSs) were originally constructed using full height transversely magnetized ferrite slabs, positioned between the broad walls of the waveguide where the microwave magnetic field is circularly polarized. For high-power applications, thinner partial-height ferrite slabs adjacent to the broad wall have the advantage of being easier to cool. A megawatt peak-power DPS circulator was examined by Helszajn and Walker [4]. They presented an analysis of the resonance regions to identify magnetizations, which minimize losses, together with experimental data on the performance of a range of ferrite materials.

The first published results of a theoretical analysis of a single full-height slab in rectangular waveguide was given by Kales [5]. More detailed analyses describing fields and higher order modes were subsequently presented [3], [6], [7]. The twin full-height slab geometry used in latching phase shifters was first analyzed by Lax *et al.* [6] with further work described in [3] and [7]–[9]. Partial-height slabs cannot be treated analytically, and numerical methods must be employed. When the cross section of the ferrite slab is small compared to the waveguide, perturbation techniques can be used to evaluate the propagation constant for the weakly magnetized case [10], [11]. In the past 20 years, the finite-element (FE) method has proven to be the most popular numerical method for analyzing ferrite loaded waveguides, although other techniques have been used such as the finite-difference-time domain method [12]. FE techniques were originally applied to ferrite-loaded waveguides by Konrad [13]. Since then, new formulations have been developed to avoid spurious modes [14] and to calculate the phase constant rather than frequency as the eigenvalue [15]. Specialized formulations for the transverse magnetization of ferrites [16], [17] and magnetization in an arbitrary direction have also been proposed [18], [19].

In this paper, the propagation characteristics of a partial-height slab DPS are presented. A combined magnetostatic/microwave FE solver is employed to calculate phase constants and transverse microwave fields in terms of frequency, bias field, and material parameters. The magnetization curve and magnetic circuit geometry are input to a magnetostatic solver to establish the spatial variation of the magnetization and internal magnetic field in the ferrite slabs. This avoids the use of demagnetizing factors and accounts for fringing effects and nonuniform fields. Variations of 20% in the bias flux density were calculated for a typical ferrite slab. This is an important result, which may explain the early onset of nonlinear effects limiting high-power DPS performance. Using this data and the microwave frequency, a full permeability tensor is then constructed for the ferrite. The waveguide cross-sectional geometry together with the ferrite tensor and dielectric properties describe the microwave problem, and this is solved using a vector FE formulation in terms of the transverse-field components. This procedure was applied to a 9.25-GHz device where differential phase shift was calculated as a function of the gap bias field. Starting from the demagnetized case through to a saturated ferrite, the calculations agreed to within 5% of measured data. Further studies indicate that slab geometry has a more significant effect on single-mode bandwidth than bias field or material properties. However, bias field and material properties play an important role in phase-constant splitting and the associated differential phase shift. Above resonance, use of the dominant mode is limited by nonsymmetrical mode splitting and reduced differential phase shift. Examination of the transverse magnetic field illustrates that the operation of the DPS is related to the classic edge-mode field displacement effect [7]–[9].

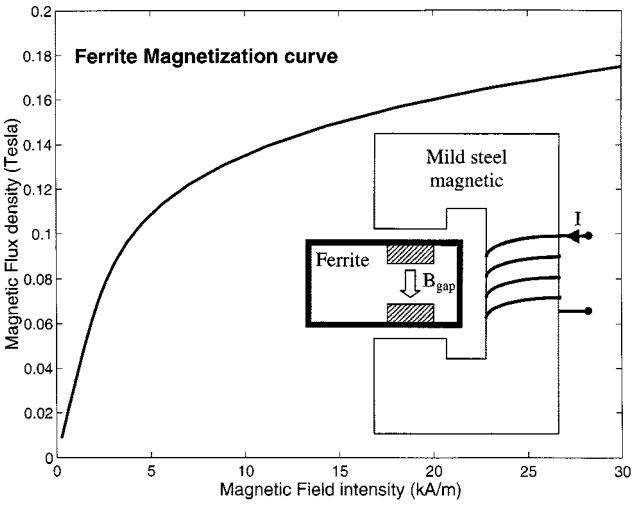

Fig. 1. Magnetization curve of ferrite. Inset is a cross section of the DPS showing the magnetic bias circuit. Waveguide size: 22.86 mm × 10.16 mm. Slab size: 7.35 mm × 2.034 mm. Offset from waveguide wall: 2.34 mm.

II. Differential Phase-Shifter Section

DPSs are used to obtain nonreciprocal phase shift in the dominant waveguide mode. The length of the ferrite-loaded waveguide section is important if the correct phase shift is to be achieved. In rectangular waveguide, the phase shifter is constructed by positioning ferrite slabs adjacent to the top and bottom sidewalls close to one of the end walls. The position coincides with the point where the alternating magnetic fields of the TE_{10} in an empty waveguide are circularly polarized. The ferrite is magnetized by a dc magnetic field perpendicular to the planes of the circularly polarized magnetic fields and the resulting tensor permeability leads to the nonreciprocal phase shift. A typical waveguide cross section is shown in the inset of Fig. 1.

Manuscript received March 24, 1999. This work was supported by EPSRC.

The authors are with the Electrical Engineering and Electronics Department, University of Manchester Institute of Science and Technology, Manchester M60 1QD, U.K. (e-mail: bernice@umist.ac.uk).

Publisher Item Identifier S 0018-9480(00)07395-6.

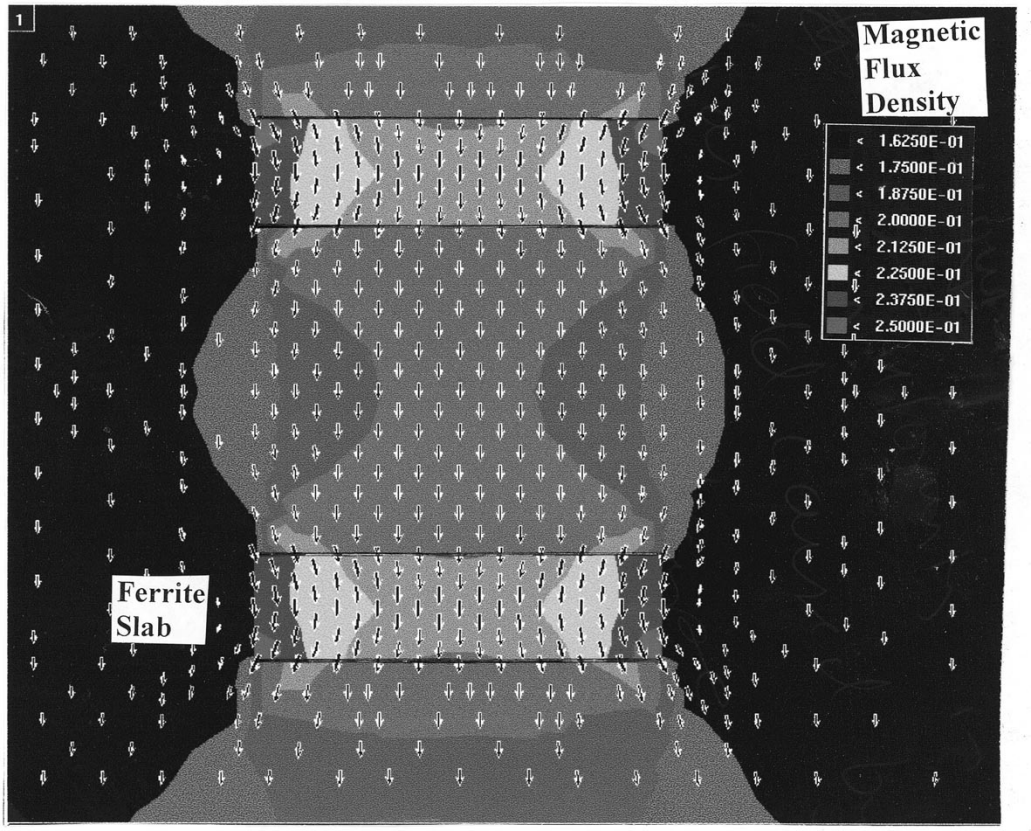

Fig. 2. Flux density $\boldsymbol{B}$ from a magnetostatic solution for waveguide cross section showing concentration around ferrite slabs. $B_{\rm gap} = 0.1896$ T.

III. Magnetostatic/Microwave FE Method

The propagation characteristics of the modes in the waveguide cross section are calculated using an FE analysis of the electric and magnetic transverse field components. The tensor values used to specify the ferrite in the waveguide are calculated from a solution of the associated magnetostatic problem.

A. Microwave Solution

Ferrite-loaded waveguides with nonuniform magnetizations support hybrid modes, which require a vector field analysis. A formulation in terms of the transverse electric ($\boldsymbol{E}_t$) and magnetic ($\boldsymbol{H}_t$) field components is used here. The coupled equations derived directly from Maxwells equations, written in terms of the radian frequency ω and the propagation constant β, are

$$\omega\epsilon\boldsymbol{E}_t - \nabla_t \times \frac{1}{\omega\mu_{zz}}[\nabla_t \times \boldsymbol{E}_t + j\omega\mu_{zt}\boldsymbol{H}_t] + \beta\hat{z} \times \boldsymbol{H}_t = 0$$

$$\omega\mu_{tt}\boldsymbol{H}_t - (-j\omega\mu_{tz}) \cdot \frac{1}{\omega\mu_{zz}}\left[\nabla_t \times \boldsymbol{E}_t + j\omega\mu_{zt}\boldsymbol{H}_t)\right] - \nabla_t \times \frac{1}{\omega\epsilon}(\nabla_t \times \boldsymbol{H}_t) - \beta\hat{z} \times \boldsymbol{E}_t = 0$$

where the permittivity ϵ is a scalar quantity and the permeability tensor has been separated into transverse and axial parts

$$\hat{\mu} = \begin{pmatrix} \mu_{tt} & \mu_{tz} \\ \mu_{zt} & \mu_{zz} \end{pmatrix}.$$

When the ferrite is magnetized in the plane perpendicular to propagation, the spatially varying tensor entries are evaluated from the signal frequency ω, the internal magnetic field $\boldsymbol{H}_i$, and the magnetization $\boldsymbol{M}$

$$\mu_{tt} = \frac{\mu_0}{\omega_d}\begin{pmatrix} \omega_d + \omega_{my}\omega_{oy} & -\omega_{mx}\omega_{oy} \\ -\omega_{my}\omega_{ox} & \omega_d + \omega_{mx}\omega_{ox} \end{pmatrix} \tag{1a}$$

$$\mu_{tz} = \mu_{zt}^* = j\frac{\mu_0}{\omega_d}\begin{pmatrix} \omega\omega_{my} \\ -\omega\omega_{mx} \end{pmatrix} \tag{1b}$$

$$\mu_{zz} = \frac{\mu_0}{\omega_d}(\,\omega_d + \omega_{my}\omega_{oy} + \omega_{mx}\omega_{ox}\,) \tag{1c}$$

where $\omega_{ox} = \gamma\boldsymbol{H}_i \cdot \hat{x}$, $\omega_{oy} = \gamma\boldsymbol{H}_i \cdot \hat{y}$, $\omega_{mx} = \gamma\boldsymbol{M} \cdot \hat{x}$, $\omega_{my} = \gamma\boldsymbol{M} \cdot \hat{y}$, $\omega_d = \omega_{ox}^2 + \omega_{oy}^2 - \omega^2$, and γ is the gyromagnetic ratio and μ_0 is the permeability of free space. No assumptions have been made regarding the uniformity of the bias field. If the applied field is assumed to be uniform, then zero entries would occur in some off-diagonal tensor values.

An FE solution of these equations is obtained by constructing a mesh over the waveguide cross section. The discretized electric and magnetic fields within each element of the region are approximated using edge variables. The solution of the discretized equations is obtained using a weighted residual approach, and this leads to an eigenvalue matrix problem of the form

$$Ax = \beta^2 Bx$$

where x is the vector of unknown field coefficients and A and B are real symmetric banded matrices.

B. Magnetostatic Solution

To evaluate the tensor entries accurately, the internal field and magnetization within the ferrite must be known. The relationship between

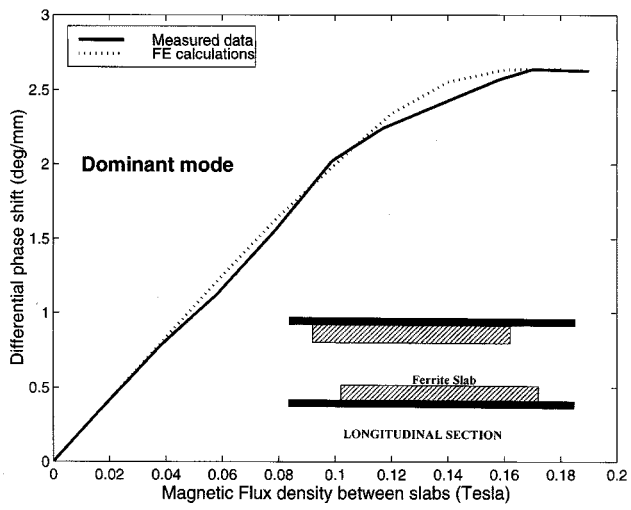

Fig. 3. Measured and calculated values for differential phase shift (degrees/millimeters) for ferrite magnetized below resonance with frequency $= 9.25$ GHz. Inset is longitudinal section of the DPS. Single-slab length: 11.43 mm. Double-slab length: 31.23 mm.

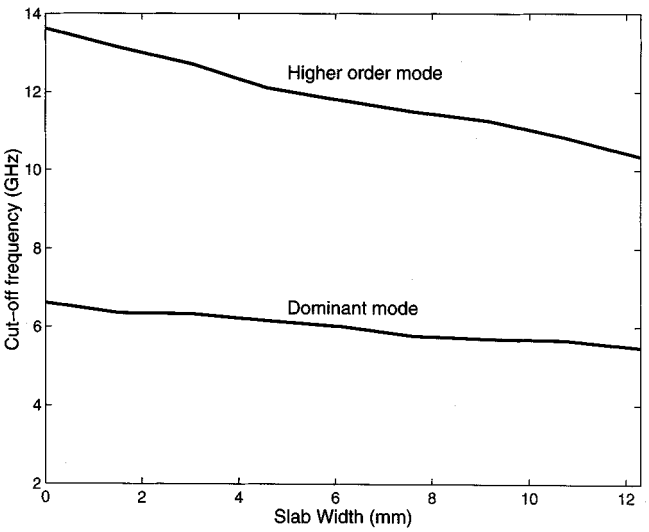

Fig. 4. Variation of cutoff frequencies with slab width. Slab height: 2.034 mm. $B_{\rm gap} = 0$.

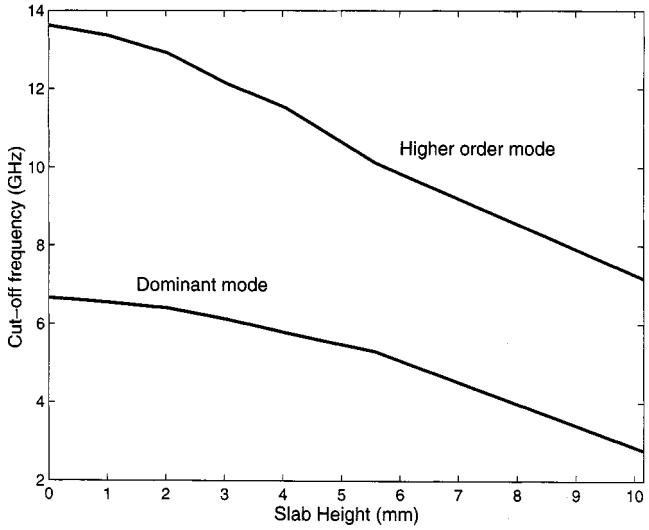

Fig. 5. Variation of cutoff frequencies with slab height. Slab width: 7.35 mm. $B_{\rm gap} = 0$.

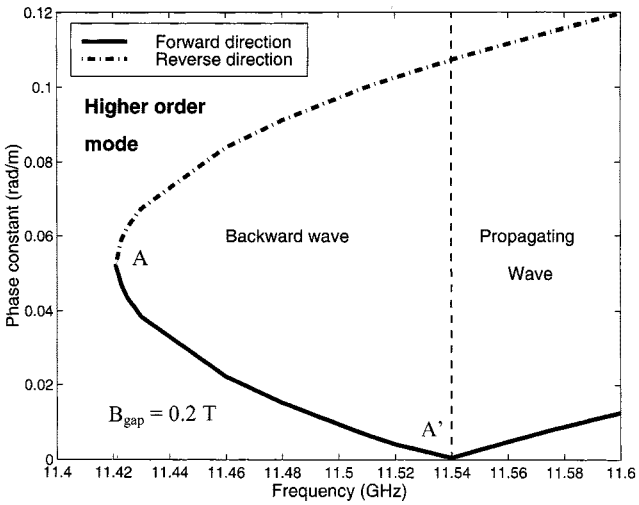

Fig. 6. Backward wave for higher order mode. $B_{\rm gap} = 0.2$ T.

these values and the applied bias field is complicated by the effect of the demagnetizing field due to the surface divergence of the magnetization vector. For nonellipsoidal ferrite shapes, the demagnetizing field is nonuniform, leading to spatially varying tensor values. Joseph and Schlomann [20] evaluated the demagnetizing field in ferrites of arbitrary shape with a uniform bias field. A magnetostatic FE solution is used here to calculate the $\boldsymbol{M}$, $\boldsymbol{H}_i$ variables directly. A mesh is constructed over the full geometry including the ferrite-loaded waveguide, magnetic material, and current windings. All materials are characterized by their permeability, and nonlinear materials such as ferrite and magnetic materials are characterized by their magnetization curves. A standard two-dimensional FE magnetostatic solver is used to solve the nonlinear Poisson equation in terms of the axial component of the magnetic vector potential ψ [21]. The flux density $\boldsymbol{B}_{\rm dc}$, field intensity $\boldsymbol{H}_i$, and magnetization $\boldsymbol{M}$ can all be evaluated from the magnetic potential ψ. Once these values are known throughout the ferrite, the tensor values can be calculated for a specific frequency using the relationship defined by (1a)–(1c).

IV. Comparison with Experiment

To verify the accuracy of the calculations, the results were compared with measured values for a DPS section.

For the FE calculations, the ferrite is completely defined by its magnetization curve and relative permittivity. The ferrite used here has a relative permittivity $\epsilon_r = 11.4$ and its magnetization curve is shown in Fig. 1. The inset of Fig. 1 is a sketch of the magnetic bias circuit showing the transverse waveguide cross section with ferrite slabs. The applied bias field $B_{\rm gap}$ in any calculation is assumed to be the magnetic flux density at the center point between the two ferrite slabs. To ensure a uniform field between the poles of the magnet, the pole face was taken to be four times the width of the ferrite. $B_{\rm gap}$ is varied by changing the current (I) in the windings of the electromagnet. The magnetic flux density in the ferrite slabs calculated by the magnetostatic solver is shown in Fig. 2. For reasons of scale, only the ferrite slabs and the air gap between them are illustrated. The concentration

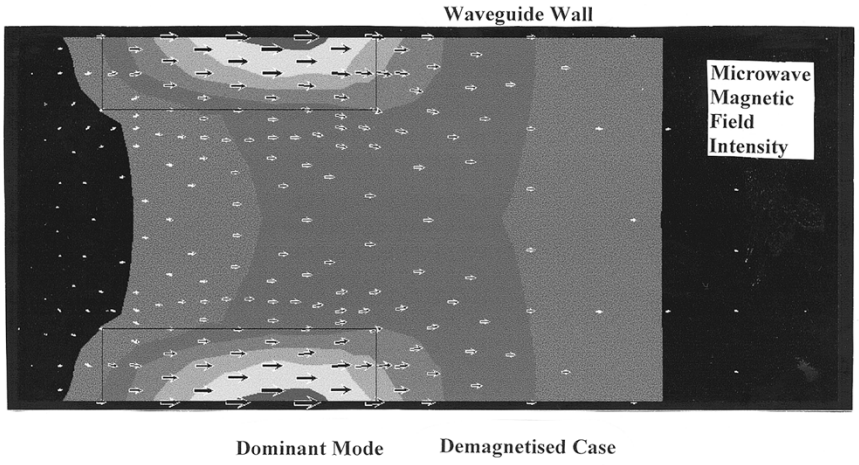

(a)

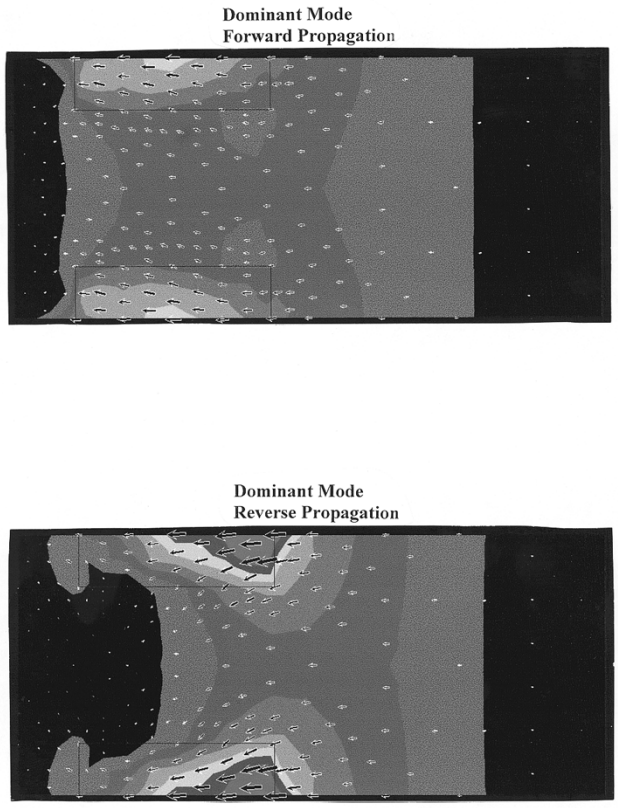

(b)

Fig. 7. Typical microwave magnetic-field intensity of dominant mode. Frequency: 9.25 GHz. (a) Unmagnetized dominant mode. (b) Forward and reverse dominant mode. $B_{\rm gap} = 0.16$ T.

and bending of the flux density at the slab corners is evident. The magnetic flux density through a cross section of the ferrite slab in Fig. 2 varies by 20%. This is a significant effect, which is often neglected in alternative analysis techniques where a uniform bias field is assumed. For example, with high-power operation, the field concentration at the slab corners can result in the onset of nonlinear effects earlier than expected.

The longitudinal waveguide cross-sectional geometry used in the microwave FE calculations is shown in the inset of Fig. 3. It is composed of two single-slab sections and a central double-slab section. The single-slab section is used as a match to the empty waveguide. FE calculations were done for the single- and double-slab section separately and the results were combined to give a differential phase shift over the length of the phase shifter for the dominant mode. This hybrid mode is related to the $\rm TE_{10}$ mode in an empty rectangular waveguide. Fig. 3 illustrates good agreement to within 5% between the measured and calculated phase shifts. A contributory factor to the error may be the accuracy in the definition of the shape of the magnetization curve.

V. Results for Typical Phase-Shifter Cross Sections

The split in the phase constants between the forward- and reverse-propagating modes is the crucial parameter in the design of DPS sec-

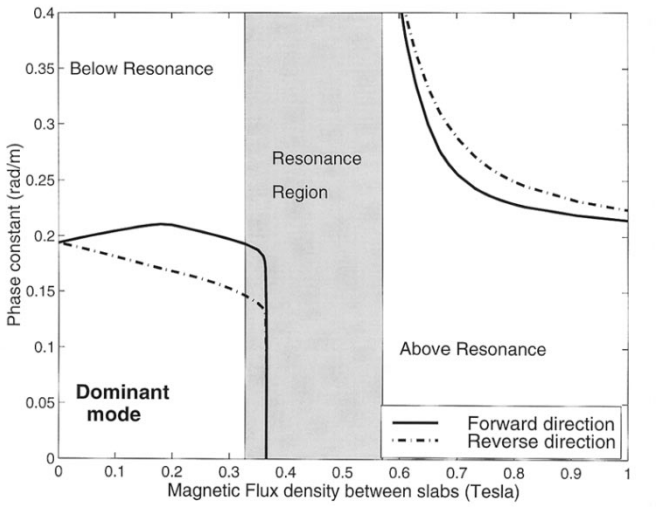

Fig. 8. Variation of phase-constant split with magnetization. The frequency is 9.25 GHz; waveguide geometry as in Fig. 1. The resonance region is defined where $\kappa/\mu > 1$.

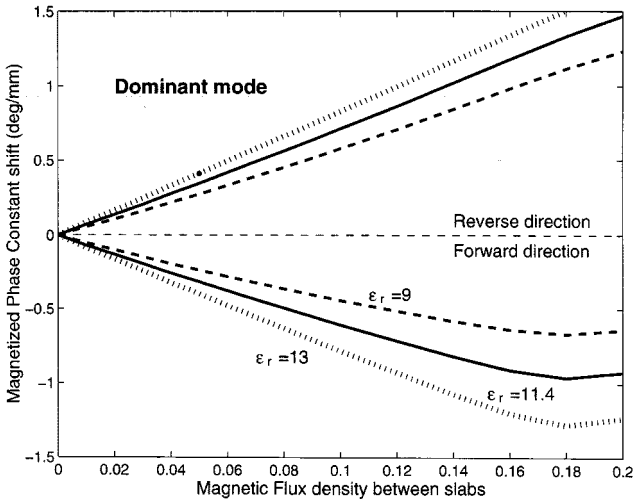

Fig. 9. Variation of phase-constant split with different dielectric permittivity of ferrite. Frequency: 9.25 GHz (waveguide geometry as in Fig. 1).

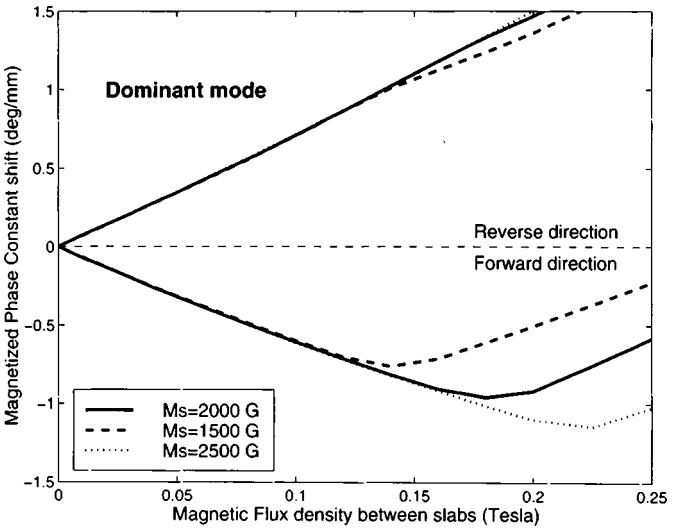

Fig. 10. Variation of phase split with different saturation magnetization values. Frequency: 9.25 GHz (waveguide geometry as in Fig. 1).

tions. To quantify the effect of various geometrical and material parameters on this split, both the cutoff and propagating planes are examined. For these calculations, saturation magnetization of $M_s = 2000$ G is used. The geometry of the waveguide cross section is identical to that illustrated in Fig. 1.

A. Cutoff Plane Calculations

Cutoff plane calculations are important to determine the frequency bandwidth available for single-mode operation. The first higher order mode for the waveguide cross-sectional geometry in Fig. 1 is a hybrid mode related to the TE_{20} mode in an empty waveguide. Fig. 4 illustrates the variation in cutoff frequency with slab width for the unmagnetized case. Increasing the slab width from 0 to 12.3 mm reduces the single-mode bandwidth from 6.6 to 5.4 GHz. Fig. 5 illustrates the variation in cutoff frequency with slab height for the unmagnetized case. As the height increases, the cutoff frequencies of both modes reduce. An octave operating bandwidth is maintained from the empty to the full-height case where the cutoff frequencies are reduced by 50%.

A study was also made of the effect of dielectric constant in the ferrite slabs. Relative permittivities from 9 to 13 have little affect on the cutoff frequencies. The dominant mode cutoff decreases by approximately 1% over this range and the higher order mode by approximately 4%.

The effect of magnetization on cutoff frequencies was then examined. For a magnetized ferrite, the frequency must be specified when calculating the tensor permeability and, thus, the modal cutoff frequencies cannot be calculated directly by setting the phase constant to zero. Using an iterative approach, the dominant and first higher order mode cutoff frequencies are found to increase slightly with increasing magnetization. For the unmagnetized geometry, the dominant mode cutoff is 5.76 GHz and that of the first higher order mode is 11.49 GHz, respectively. These increased to 5.95 and 11.54 GHz when the gap bias field (B_{gap}) is increased to 0.2 T.

Analysis of the cutoff planes of strongly magnetized ferrites also reveals the existence of split cutoff frequencies for reverse- and forward-propagating modes. The frequency split increases with magnetization, and backward wave propagation is found to exist within the split cutoff frequencies. This effect is more pronounced for the higher order mode, which has a backward-wave bandwidth of 0.12 GHz when $B_{\mathrm{gap}} = 0.2$ T, whereas the dominant mode backward wave bandwidth is only 0.05 GHz. Fig. 6 illustrates the variation of phase constant with frequency for the higher order mode with this gap field. At 11.43 GHz (A), the mode first appears, but the forward-propagating mode has a decreasing phase constant typical of backward waves $(A$–$A')$. At 11.54 GHz (A'), the mode reverts to a typical propagating mode. The existence of backward waves in magnetized ferrites has been noted previously by other authors [22], [7].

B. Propagating Plane Calculations

When the ferrite is demagnetized, each pair of forward- and reverse-propagating modes have the same phase constants, transverse electric variation, and magnetic field variation. Fig. 7(a) illustrates the transverse magnetic field for the dominant mode when the ferrite is unmagnetized. The field is concentrated in the ferrite slabs due to the higher relative permittivity. With a magnetized ferrite, the magnetic fields of the forward- and reverse-propagating modes couple differently with the internal magnetic field and this gives rise to the edge-mode effect clearly discernible in the magnetic fields of Fig. 7(b). This shifting of the field concentration toward the slab edge in *one* of the modes and the associated split phase constants give the ferrite slabs their nonre-

ciprocity. The edge-mode field displacement effect and the split phase constants increase with the gap bias field until it is a maximum at saturation. Increasing the magnetization further does not increase the differential phase shift. Fig. 8 illustrates the forward- and reverse-propagating phase constants as a function of magnetization at a fixed frequency. A resonance region where the electromagnetic energy is lost to the ferrite is shown. In the resonance region, the calculated dominant mode cuts off, however, many other modes exist. Above resonance, the split phase constant is reduced, decreases with increasing magnetization, and no longer symmetrical. The operation point in the DPS is usually chosen to be close to the saturation magnetization below the resonance region.

The size of the phase-constant split can be increased by increasing the dielectric permittivity, as shown in Fig. 9. At $B_{\rm gap} = 0.18$ T, the differential phase split between the forward- and reverse-propagating modes increases by 56% when the relative permittivity is changed from 9 to 13. Increasing the saturation magnetization of the material will also result in a larger split. Fig. 10 shows the forward and reverse split for three different materials. These materials were simulated using the same magnetization curve, but by changing M_s value. At $B_{\rm gap} = 0.225$ T, the differential phase split between the forward- and reverse-propagating modes increases by 49% when the M_s value increases from 1500 to 2500 G.

VI. Conclusions

Rectangular waveguide loaded with ferrite slabs is a classic arrangement for high-power DPSs. The FE procedure proposed here is used to evaluate the differential phase shift as a function of bias field for a fixed geometry, signal frequency, and ferrite internal properties. The magnetostatic solution revealed typical variations of 20% in bias flux density within the ferrite slab—this result may explain the early onset of nonlinear effects in high-power DPSs. A direct comparison of differential phase shift with an experimental 9.25-GHz device validated the numerical calculations to within 5%. Bias field and relative permittivity were found to have little effect on the cutoff plane of the phase shifter. Differential phase shift is improved by increasing magnetization and relative permittivity. Above resonance operation is restricted by nonsymmetrical splitting and lower differential phase shift. Information on backward-wave propagation and field plots were included for completeness.

Acknowledgment

The author would like to acknowledge the help and support of TRAK Microwave Ltd., Dundee, U.K., for providing the experimental data.

References

[1] C. L. Hogan, "The ferromagnetic Faraday effect at microwave frequencies and its applications," *Bell Syst. Tech. J.*, vol. 31, pp. 1–31, 1952.
[2] A. G. Fox, S. E. Milles, and M. T. Weiss, "Behavior and application of ferrites in the microwave region," *Bell Syst. Tech. J.*, vol. 34, pp. 5–103, 1955.
[3] B. Lax and K. J. Button, *Microwave Ferrites and Ferrimagnetics*. New York: McGraw-Hill, 1962.
[4] J. Helszajn and P. N. Walker, "Operation of high peak power differential phase shift circulators," *IEEE Trans. Microwave Theory Tech.*, vol. MTT-26, p. 9, Sept. 1978.
[5] M. L. Kales, H. N. Chait, and N. G. Sakiotis, "A nonreciprocal microwave component," *J. Appl. Phys.*, vol. 24, pp. 816–817, 1953.
[6] B. Lax, K. J. Button, and L. M. Roth, "Ferrite phase shifters in rectangular waveguide," *J. Appl. Phys.*, vol. 25, pp. 1413–1421, 1954.
[7] J. Helszajn, *Principles of Microwave Ferrite Engineering*. New York: Wiley, 1969.
[8] P. J. B. Clarricoats, *Microwave Ferrites*. London, U.K.: Chapman & Hall, 1961.
[9] R. A. Waldron, *Ferrites*. New York: Van Nostrand, 1961.
[10] B. Lax, "Frequency and loss characteristics of microwave ferrite devices," *Proc. IRE*, vol. 44, pp. 1368–1386, 1956.
[11] E. Schlomann, "On the theory of the ferrite resonance isolator," *IRE Trans. Microwave Theory Tech.*, vol. MTT-8, pp. 199–206, Mar. 1960.
[12] B. S. Yildirim and E. B. El-Sharawy, "Finite-difference time domain analysis of a stripline disc junction circulator," in *IEEE MTT-S Int. Microwave Symp. Dig.*, June 1998, Paper WE2E-4, pp. 629–632.
[13] A. Konrad, "Vector variational formulation of electromagnetic fields in anisotropic media," *IEEE Trans. Microwave Theory Tech.*, vol. MTT-24, pp. 553–559, Sept. 1976.
[14] A. Bossavit and I. Mayergoyz, "Edge elements for scattering problems," *IEEE Trans. Magn.*, vol. 25, pp. 2816–2821, July 1989.
[15] J. F. Lee and Z. J. Csendes, "Full-wave analysis of dielectric waveguides using tangential vector elements," *IEEE Trans. Microwave Theory Tech.*, vol. 39, pp. 1262–1271, Aug. 1991.
[16] T. Angkaew, M. Matsuhara, and N. Kumagai, "Finite-element analysis of waveguide modes: A novel approach that eliminates spurious modes," *IEEE Trans. Microwave Theory Tech.*, vol. MTT-35, pp. 117–123, Feb. 1987.
[17] G. Forterre, P. H. Giesbers, and E. Laroche, "Finite element analysis of ferrite-loaded transmission lines," *IEEE Trans. Magn.*, vol. MAG-23, pp. 2666–2667, Sept. 1987.
[18] B. C. Anderson and Z. J. Cendes, "Solution of ferrite-loaded waveguide using vector finite elements," *IEEE Trans. Microwave Theory Tech.*, vol. 31, pp. 1578–1581, May 1995.
[19] L.-Z. Zhou and L. E. Davis, "Finite-element method with edge elements for waveguides loaded with ferrite magnetized in arbitrary direction," *IEEE Trans. Microwave Theory Tech.*, vol. 44, pp. 809–815, June 1996.
[20] R. I. Joseph and E. Schlomann, "Demagnetizing field in nonellipsoidal bodies," *J. Appl. Phys.*, vol. 36, pp. 1579–1593, May 1965.
[21] *SLIM User's Manual*, GEC Alsthom Eng. Res. Ctr., 1992.
[22] R. A. Waldron, "Properties of ferrite-loaded cylindrical waveguides in the neighborhood of cut-off," *Proc. Inst. Elect. Eng.*, pt. B, vol. 109, pp. 90–94, 1962.

Improved Microwave Performance on Low-Resistivity Si Substrates by Si^+ Ion Implantation

Pin-Quan Chen and Yi-Jen Chan

***Abstract*—Microwave characteristics of spiral inductors on low-resistivity Si substrates have been improved by implanting Si^+_{28} ions. Spiral inductors fabricated on these implanted substrates demonstrate better Q-value and microwave performance. The Q-value of inductor enhanced 60% on the implanted substrates than that of low-resistivity Si substrates. An equivalent circuit model of inductor has been evaluated to discuss the effect of substrate loss.**

I. Introduction

Monolithic microwave integrated circuit (MMIC) designs on Si substrates have become an important topic in recent years. By improving the process technologies, Si-based active devices, MOSFET's and BJT's for example, demonstrate an extremely high f_t and $f_{\max}$, which is sufficient for microwave applications. However, it is relatively difficult to realize high-Q passive elements on low-resistivity (low-R)

Manuscript received May 21, 1999. This work was supported by the National Science Council, R.O.C., under Contract NSC 87-2218-008-024.

The authors are with the Department of Electrical Engineering, National Central University, Chungli, Taiwan 32054, R.O.C.

Publisher Item Identifier S 0018-9480(00)07397-X.

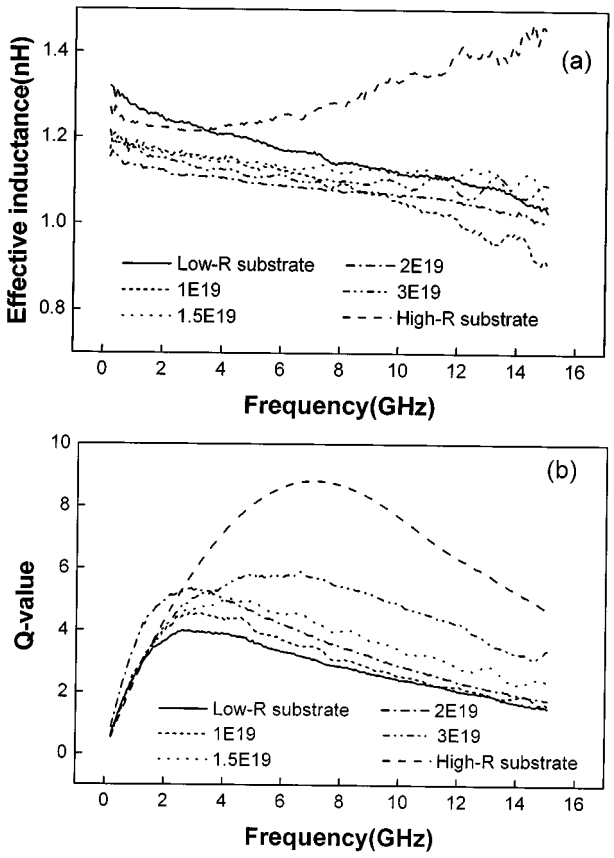

Fig. 1. (a) Calculated effective inductance and (b) Q-values of the 1.5-turn spiral inductors fabricated on implanted Si substrates, low-resistivity Si substrates, and high-resistivity Si substrates (from 45 MHz to 15 GHz).

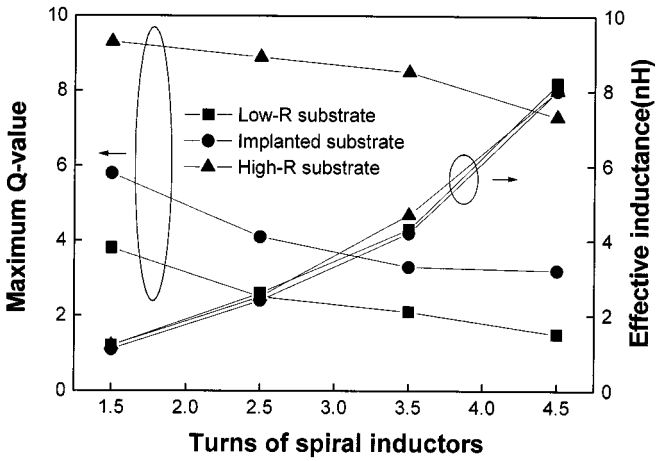

Fig. 2. Q-value and effective inductance at 900 MHz versus turns of spiral inductors on Si implanted (concentration: 3×10^{19} cm^{-3}), low-R, and high-R substrates.

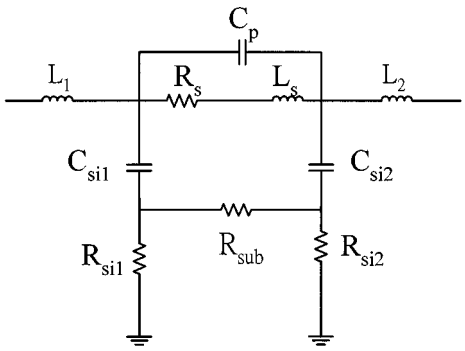

Fig. 3. Equivalent circuit model of spiral inductor on Si substrates.

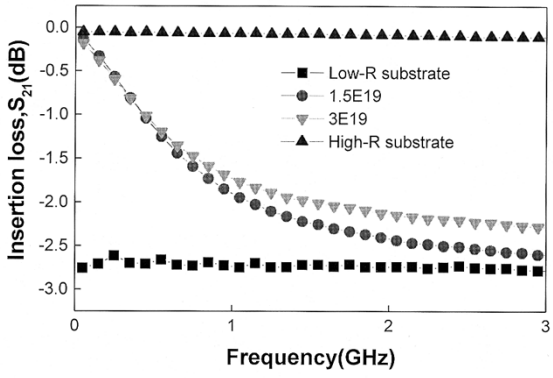

Fig. 4. Measured S_{21} insertion loss of a 600-μm-long through line on different prepared substrates.

Si substrates because of the nature loss under the microwave operation. Among them, the spiral inductor, which is extensively used in biasing and matching circuits, is the main issue to resolve this low-Q problem. Many approaches have been proposed to achieve better microwave performance of inductors on low-R Si substrates, including inductors with a pattern ground shielding [1], with multi-layer metals [2]–[5], or by inserting a thick polymide layer [6]. These solutions are basically focused on reducing substrate conduction and loss, resulting in an elimination of wave propagation loss in the substrate, and therefore improving the associated Q-value.

Ion implantation technology has been proposed to reduce the loss of Si substrate through a high-resistivity surface layer by disordering the lattice sites [7]. In this paper, we systematically implanted Si_{28}^{+} into conventional low-R Si substrates ($\rho \sim 5$–$10\ \Omega$·cm) to damage the Si lattice structure, and an amorphous layer will be formed subsequently on the surface of Si substrates. The thickness of this surface amorphous layer varies with different implant energies and doses, which can be estimated by the LSS simulator. In this study, spiral inductors were fabricated on the implanted Si substrates. By measuring the microwave characteristics of spiral inductors, we can evaluate the performance improved through this implantation technology. For comparisons, we also fabricated the spiral inductors on the high-resistivity (high-R) Si substrate, where resistivity is 4 kΩ·cm. In addition, through lines (600 μm-long) were fabricated on these Si substrates. By measuring the S_{21}, the insertion loss resulting from the substrate effect can also be determined.

II. Implantation Conditions and Fabrication of Spiral Inductor

The maximum energy of the ion implanter is 200 keV with an ion source of SiH_4. A multi-implantation approach was used to realize a uniform distribution of implanted profile for a depth of 0.4-μm thick, which is limited by the implanter maximum energy. We systematically changed implanted Si concentrations from 1×10^{19} cm^{-3} to 4×10^{19}

TABLE I
EXTRACTED PARAMETERS CORRESPONDING TO THE INDUCTOR EQUIVALENT CIRCUIT MODEL (INDUCTOR WITH A 1.5-TURNS)

	C_{si1} (pF)	C_{si2} (pF)	R_{sub} (kΩ)	R_{si1} (Ω)	R_{si2} (Ω)	R_s (ohm)	L_s (nH)	C_p (pF)	L_1 (nH)	L_2 (nH)	Q_{max}
Low-R	7.3	8.8	7.4	206	177	2.9	1.2	7E-3	1E-4	6E-4	3.8
1E19	1.3	1.2	40	152	183	2.6	1.2	2E-3	1E-1	2E-2	4.5
1.5E19	1.3	0.9	100	105	261	3	1.1	1E-3	0	0	5
2E19	0.8	1.0	200	178	155	2.6	1.1	1E-2	1E-3	1E-3	5.3
3E19	0.5	1.1	900	296	168	2.3	1	1E-3	0	2E-1	5.8
4E19	0.5	1.5	1000	188	153	2.6	0.9	1E-2	5E-2	2E-2	5.2
High-R	0.03	0.04	*	71	30	3.3	1	1E-1	6E-2	1E-3	9.3

*: not necessary of this R_{sub} in the equivalent circuit of high-R substrate.

cm^{-3} to evaluate how this damage layer affects the microwave performance.

After the realization of the implanted substrates, the square-shaped spiral inductors were subsequently fabricated on the substrate by using air-bridge technology, which can minimize the parasitic capacitance between the cross over metal lines. The Au metal lines were deposited by electroplating, and the thickness is about 6 μm to reduce the loss from ohmic conduction. The metal line-width and spacing are all 25-μm wide in our spiral inductor design. The inner diameter of inductors is 130 μm.

III. EXPERIMENTAL RESULTS AND DISCUSSIONS

The spiral inductors are designed for a direct two-port S-parameter evaluation. Microwave S-parameters (from 45 MHz to 15 GHz) were measured by an HP8510C network analyzer in conjunction with on-wafer G-S-G coplanar Cascade probes. The de-embedding work has to be done first on Si substrates in order to remove the parasitic effects from probe pads and feeding lines. The two-port S-parameters were first transferred into one-port S-parameters by terminating a 50 □ load on the output ports, and the subsequent Z-parameters can be calculated. Based on the real and imaginary parts of Z-parameters, the effective resistance (real part) and inductance (imaginary part) versus frequencies can be extracted [8]. The associated Q-value can also be obtained. Fig. 1(a) and (b) shows the effective inductance and the Q-value of spiral inductors fabricated on low-R Si substrates, implanted substrates, and high-R substrates, respectively. These spiral inductors are 1.5 turns with a metal thickness of 6 μm. The bias voltage for a 2-mA leakage current between two metal lines (100-μm wide separation) is 2.5 V for a low-R Si substrate; however, this value is above 200 V for the implanted substrate (concentration: 3×10^{19} cm^{-3}). It indicates that Si_{28}^{+} implantation technology is a sufficient way to create a high-resistivity surface layer. The effective inductance is around 1.1 nH for inductors fabricated on all kinds of substrates, and this value is relatively insensitive to frequencies up to 15 GHz. As to the effective resistance, inductors on implanted substrates show lower values than those on low-R Si substrates. Due to a higher conducting loss at high frequencies, effective resistances increases versus frequencies. As we can see in Fig. 1(b), at low frequencies, the Q-values increase versus frequencies, which is determined by the ohmic conducting mechanism. However, Q-values move downward by further increasing the frequencies, which is associated with substrate parasitic effect dominating at higher frequencies. It therefore forms a peak Q-value in Fig. 1(b). The peak Q-values shift to high-frequency end at implanted and high-R substrates, which is associated with a reduced substrate parasitic effect causing this shift. The maximum Q-value of inductor on low-resistivity Si substrate is 3.8, and it reaches 5.8 as the implant concentration increases to 3×10^{19} cm^{-3}. The Q-value slightly reduces to 5.2 for the implant concentration of 4×10^{19} cm^{-3}. This slight decrease of Q-value maybe correspondent to the self-annealing effect within the damaged layer in high dose substrates, alleviating the degree of damaged crystalline. Therefore, it translates that the optimum ion concentration for the enhancement of microwave performance for spiral inductor is about 3×10^{19} cm^{-3}. As to the high-R Si substrate, the maximum Q-value is 9.3, which is much higher than those of implanted substrates.

Spiral inductors fabricated on different prepared Si substrates with various turns were also investigated, and results are shown in Fig. 2. The peak Q-values decrease by increasing the turn number of spiral inductors, which is associated with the increase of conducting loss and the associated parasitic capacitance from the substrate. For a concentration of 3×10^{19} cm^{-3}, the peak Q-value with a 4.5-turns drops to 3.2. This Q-value drop is more significant in the case of low-R substrates, where the substrate parasitic effect is more severe. However, Q-value reduction versus inductor-turns is negligible on high-R substrates. The effective inductances obtained at 900 MHz are similar for these three different substrates and demonstrate a systematic increase vs. inductor-turns. A maximum inductance of 8 nH is obtained for a 4.5-turns inductor, and this value is enough for a practical MMIC design.

In addition to direct calculations from measured S-parameters, we also establish an equivalent circuit model shown in Fig. 3. For these spiral inductors, the equivalent circuit model provides an analytic tool to identify the improving factors caused by this ion implantation approach. The elements of the equivalent circuit model listed in Table I were extracted from curve-fitting procedure of the two-port S-parameters (from 50 MHz to 7 GHz) of an inductor with a 1.5 turn on various prepared substrates. This fitting process was executed by HP MDS software. $R_{\rm sub}$ refers to the substrate resistance, and $C_{\rm si}$ is associated with the grounding capacitance. These two elements represent mainly the substrate parasitic effect. During the curve fitting, we observed that $R_{\rm sub}$ of inductor on a high-R Si substrate is not necessary, which translates that the substrate loss of high-R substrate is negligible. The $R_{\rm sub}$ of an inductor on a low-R Si substrate is about 7.4 kΩ, and this value enhances to 900 kΩ for an implant concentration of 3×10^{19} cm^{-3} substrate. The average $C_{\rm si}$ of implanted substrates is also improved to 0.8 pF, as compared with the original average 8 pF on low-R substrates. Therefore, it suggests that the implanted layers indeed improve the Si substrate loss and parasitic capacitance, resulting in a higher Q-value and better frequency response of spiral inductors.

A 600-μm-long through line was also fabricated for a direct two-port measurement to evaluate the transmission-line loss

through the different Si substrates. This through line is designed for a 50-Ω input impedance based on the high-resistivity Si substrate. S-parameters of these through lines on different prepared substrates were evaluated. As seen in Fig. 4, the S_{21} insertion loss of the through line on a low-R Si substrate are all below 2.5 dB within the measured frequency band. As to the implanted substrates, the insertion loss is small at low frequencies and starts to increase at the high-frequency end. By increasing the implant concentration, the microwave substrate loss has been improved. Through lines on a high-R substrate show a great microwave performance where the insertion loss is below 0.1 dB at frequencies up to 3 GHz. Although the improved microwave performance can be obtained from the implanted substrate, the substrate parasitic effect, such as $R_{\rm sub}, C_{\rm si}$, cannot be as good as the results from high-R substrates, which are due to the thickness limitation of implant-damaged layers.

IV. Conclusion

In summary, by creating an implant-damaged layer on low-resistivity Si substrates, the microwave performance of the spiral inductors can be improved. This technology provides a high resistive surface layer resulting in a higher Q-value and a lower parasitic effect of spiral inductors. The microwave performance of Si substrate is systematically improved and reaches an optimum implant concentration of 3×10^{19} cm^{-3}. However, by using the conventional implanter, due to the limitation of implant energy, the damaged layer is too thin to prevent the all loss from the substrate. Since this approach is compatible with IC technologies, by further increasing the implant energy, ion implant technologies are very attractive for Si MMIC applications.

Acknowledgment

The authors are grateful to the Optical Science Center, National Central University, for ion implantation work.

References

[1] C. P. Yue and S. S. Wong, "On-chip spiral inductors with patterned ground shields for Si-based RF IC's," *IEEE J. Solid-State Circuits*, vol. 33, pp. 85–86, Jan. 1998.

[2] M. Soyuer, J. N. Burghartz, K. A. Jenkins, and S. Ponnapalli, "Multilevel monolithic inductors in silicon technology," *Electron. Lett.*, vol. 31, pp. 359–360, 1995.

[3] J. N. Burghartz, M. Soyuer, and K. A. Jenkins, "Microwave inductors and capacitors in standard multilevel interconnect silicon technology," *IEEE Trans. Microwave Theory Tech.*, vol. 44, pp. 100–104, Jan. 1996.

[4] J. N. Burghartz, M. Soyuer, K. A. Jenkins, and M. D. Hulvey, "High-Q inductor in standard silicon interconnect technology and its application to an integrated RF power amplifier," in *Int. Electron Devices Meeting Tech. Dig.*, 1995, pp. 1015–1017.

[5] R. B. Merrill, T. W. Lee, H. You, R. Rasmussen, and L. A. Moberly, "Optimization of high-Q integrated inductors for multi-level metal MOS," in *Int. Electron Devices Meeting Tech. Dig.*, 1995, pp. 983–986.

[6] B. K. Kim, B. K. Ko, and K. Lee, "Monolithic planar inductor and waveguide structure on silicon with performance comparable to those in GaAs MMIC," in *Int. Electron Devices Meeting Tech. Dig.*, 1995, pp. 712–720.

[7] C. P. Liao, T. H. Huang, C. Y. Lee, D. Tang, S. Ming, T. N. Yang, and L. F. Lin, "Method of creating local semi-insulating regions on silicon wafers for device isolation and realization of high-Q inductors," *IEEE Electron Device Lett.*, vol. 19, pp. 461–462, 1998.

[8] S. Chaki, S. Aono, N. Andoh, Y. Sasaki, N. Tanino, and O. Ishihara, "Experimental study on spiral inductors," in *IEEE MTT-S Int. Microwave Symp. Dig.*, 1995, pp. 753–756.

Asymmetric Four-Port and Branch-Line Hybrids

Hee-Ran Ahn and Ingo Wolff

***Abstract*—Two different asymmetric branch-line hybrids, a conventional-direction asymmetric branch-line hybrid (CABH) and an anti-conventional-direction asymmetric branch-line hybrid (AABH) are discussed and their design equations are derived. On the basis of the derived design equations, a uniplanar CABH was fabricated with coplanar wave guide (CPW) technology and measured.**

***Index Terms*—AABH, asymmetric branch-line hybrids, asymmetric four-port hybrids, CABH.**

I. Introduction

Ring hybrids and branch-line hybrids are of primary importance in microwave integrated circuits. Historically, the first ring hybrid was described by Tyrrel in 1947 [1]. Since that time, ring hybrids have been investigated by a number of engineers [2]–[12]. On the other hand, branch-line hybrids have been studied for a long time separately from the ring hybrids [13]–[20]. These studies on ring hybrids and branch-line hybrids focus on symmetric four-port hybrids where the conventional even- and/or odd-mode excitation analyses can be used [21]. Additionally, the relation between ring hybrids and branch-line hybrids has never been considered. As these four-port hybrids are used with active elements and/or other passive elements, additional matching circuits are necessary to obtain the desired output performances. In these cases, if these four-port hybrids are terminated by arbitrary impedances, the total size of integrated microwave circuits can be reduced [22]–[24]. Recently, for the first time, Ahn *et al.* treated asymmetric four-port ring hybrids [22], [23] and described very briefly the conventional-direction asymmetric branch-line hybrid (CABH) [24].

In this paper, the relation between an asymmetric ring hybrid (ring hybrid with arbitrary power divisions and arbitrary termination impedances) and two asymmetric branch-line hybrids (branch-line hybrids with arbitrary power divisions and arbitrary termination impedances) are discussed depending on their power division characteristics. From the relation, the design equations of the two asymmetric branch-line hybrids are derived using the method given by Ahn *et al.* [22]. Also, it is shown that the derived design equations are used not only for conventional branch-line hybrids but also for conventional impedance transformers using the one-stage branch-line [18]–[20]. On the basis of the derived design equations, a uniplanar CABH is designed with a power split ratio of 3 dB and measured.

II. Analyses

Fig. 1 shows three four-port hybrids terminated by arbitrary impedances. If one of four ports is isolated in the case of port ① excitation, there are three different cases as seen in Fig. 1. In Fig. 1(a), the power excited at port ① is split between two output ports, ② and ④, while port ③ is isolated. The two output signals are in-phase or out-of-phase depending on the input-port chosen. This application is defined as an asymmetric ring hybrid and sufficiently discussed in [22], [23]. While

Manuscript received June 22, 1999. This work was supported by Deutsche Forschungsgemeinschaft (DFG).

The authors are with the Department of Electrical Engineering, Gerhard-Mercator University Duisburg, Duisburg D-47048, Germany.

Publisher Item Identifier S 0018-9480(00)07400-7.

the above-mentioned asymmetric ring hybrid has 0° or 180° phase difference between the two output signals, the signals at the two output ports in Fig. 1(b) and (c) have 90° phase difference. These two kinds of hybrids are the so-called asymmetric branch-line hybrids.

The power division characteristic of the branch-line hybrid in Fig. 1(b) is as same as that of the conventional branch-line hybrid [13]–[20]. Thus, it may be named a *conventional-direction asymmetric branch-line hybrid* (CABH). On the other hand, the power division direction of the branch-line hybrid in Fig. 1(c) is reverse. For this reason, this asymmetric branch-line hybrid may be named an *anti-conventional-direction asymmetric branch-line hybrid* (AABH). It will be shown that the design equations of these two asymmetric branch-line hybrids are different from each other. However, from Fig. 1, it may be recognized that these CABH, AABH, and ring hybrid are in principle the same in their function. Therefore, under the assumption of $|S_{41}| = 0$, the equivalent circuit of port ① excitation may be constructed in Fig. 2 [22]. In the case of Fig. 2(a), when the power is excited at port ①, the voltage across a load R_b is equal to that across the transmission line with a characteristic impedance Z_2 and a load R_c. Therefore, if the ratio of $|S_{21}|$ to $|S_{31}|$ is required that of d_1 to d_2 as defined in Fig. 2(a), the impedance looking into the transmission line with Z_2 loaded with R_c, *In* ③ should be $(d_1^2/d_2^2)\cdot R_b$ as indicated in Fig. 2(b). In case of a Y-junction device [25], [26], such as a Wilkinson three-port power divider, an isolation resistor is necessary to isolate between two output ports and to complete matches at the two out-ports which are connected with an isolation resistor. For the asymmetric ring hybrid shown in Fig. 1(a), two arms with Z_2 and Z_3 are connected with two output ports ② and ④ for the isolation between the two output ports and perfect matches at these two outports. In case of the CABH in Fig. 1(b), the two arms with Z_3 and Z_4 are connected with the two output ports ① and ③ in order that no power is transported to port ④ and two ports ① and ③ are matched when the power is excited at port ①. Therefore, the total power excited at port ① is delivered to port ② and the power reached at port ② is divided into the load R_b at port ② and the load R_c at port ③ in Fig. 2(a). In the practical situation of Fig. 1(b), a very small amount of the excited power at port ① reflects into port ④ and also an extremely small amount of the power delivered at port ③ is traveling into port ④. In order that the port ④ is isolated from the excited power and perfect matchings appear at port ② and ③, the phase difference between the two waves must be 180° against each other and the scattering parameter ratio of $|S_{14}|$ to $|S_{34}|$ must be d_2 to d_1. In the case of the asymmetric ring hybrid in Fig. 1(a), an isolated port ③ is placed between the two output ports ② and ④. Therefore, the two output signals are either in equal phase or in 180° phase difference. In the case of the CABH, if port ④ is needed to be isolated from the power excited at port ①, the phase difference of the transmission arc length, $(\Theta_1 + \Theta_2 + \Theta_3 - \Theta_4)$ must be $\pm 180°$. For a real impedance to be transformed to another real impedance R_a using a transmission line with Z_1 as shown in Fig. 2(b), the electrical length Θ_1 of the transmission line must be 90° or odd multiples of 90°. In the same way, that of Θ_2 in Fig. 2(a) must also be 90° or odd multiples of 90°. Therefore, all transmission line lengths must be $\lambda/4$'s or odd multiples of $\lambda/4$'s. Thus, the phase difference between the two output signals at ports ② and ③ is 90° or odd multiples of 90° in Fig. 2(a). Thus, if $\Theta_1 = \Theta_2 = \pi/2$, the characteristic impedances of the CABH are

$$Z_1 = \sqrt{\frac{d_1^2}{d_1^2 + d_2^2}}\sqrt{R_a R_b}, \quad Z_2 = \frac{d_1}{d_2}\sqrt{R_b R_c}. \tag{1}$$

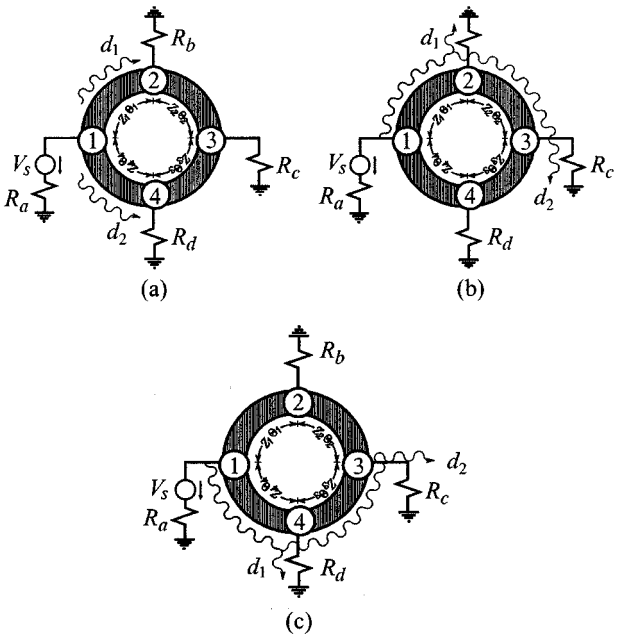

Fig. 1. Three power division representations of asymmetric 4-port hybrids in case of a port ① excitation. (a) The power division between port ② and port ④. (b) The power division between port ② and port ③. (c) The power division between port ③ and port ④.

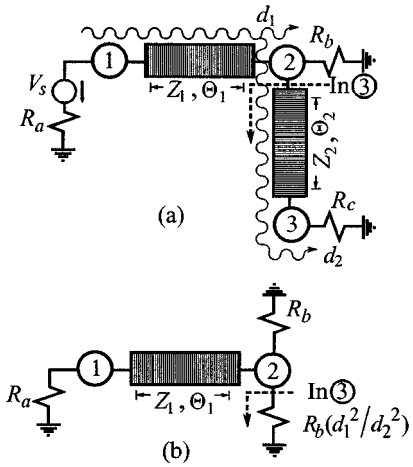

Fig. 2. The excitation at port ① in case of Fig. 1(b). (a) Under assumption of $|S_{41}| = 0$. (b) Simplifying of Fig. 2(a).

From the condition of satisfying the assumption of $|S_{41}| = 0$ [22], the two characteristic impedances Z_3 and Z_4 may be derived as

$$Z_3 = \sqrt{\frac{d_1^2}{d_1^2 + d_2^2}}\sqrt{R_c R_d}, \quad Z_4 = \frac{d_1}{d_2}\sqrt{R_d R_a}, \tag{2}$$

where the ratio of d_1 to d_2 is the scattering parameter ratio between the two output ports in Fig. 2(a), and R_a, R_b, R_c and R_d are termination impedances.

From the derived design equations (1) and (2), in case of $R_a = R_b = R_c = R_d$ and $d_1 = d_2$, the results are recognized as those of the well-known 3-dB branch-line hybrid [27], [28]. In the case of $d_1 = d_2$, the results are equal to those reported by [24]. The branch-line hybrid has been used as an impedance transformer [18]–[20]. In the case of

TABLE I
DATA OF THE REALIZED CABH WITH A POWER SPLIT RATIO 3 dB AND $\Theta_1 = \Theta_2 = \Theta_3 = \Theta_4 = 90°$ AT DESIGN FREQUENCY OF 3 GHZ. W: CENTER STRIP WIDTH, G: GAP WIDTH AND l: LINE LENGTH.

Termination impedances	Coplanar feeding transformer lines	Coplanar branch transmission lines
$R_a = 30\,\Omega$	$Z_{01} = 38.73\,\Omega$ w = 710 μm, g = 109 μm, l = 11222 μm	$Z_1 = 34.63\,\Omega$ w= 1049 μm, g = 99 μm, l = 11268 μm
$R_b = 60\,\Omega$	$Z_{02} = 54.77\,\Omega$ w = 1261 μm, g = 482 μm, l = 12185 μm	$Z_2 = 69.20\,\Omega$ w = 289 μm , g = 339 μm, l = 11001 μm
$R_c = 40\,\Omega$	$Z_{03} = 44.72\,\Omega$ w = 512 μm, g = 156 μm, l = 10879 μm	$Z_3 = 36.50\,\Omega$ w= 879 μm, g = 104 μm, l = 11207 μm
$R_d = 50\,\Omega$	$Z_{04} = 50.00\,\Omega$ w = 407 μm, g = 174 μm, l = 10869 μm	$Z_4 = 54.71\,\Omega$ w= 216 μm, g = 138 μm, l = 10681 μm

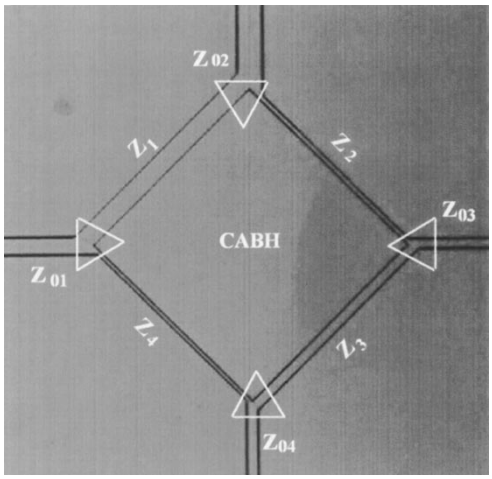

Fig. 3. Layout of a coplanar CABH with a power split ratio of 3 dB terminated by 30 Ω, 60 Ω, 40 Ω and 50 Ω.

a conventional impedance transformer using a one-stage branch-line hybrid, if $R_a = R_d = Z_{01}, R_b = R_c = Z_{02}$ and the coupling factor is defined as $|S_{31}|/|S_{21}| = d_2/d_1 = k$, the results are equal to those derived by [19], where Z_{01} and Z_{02} are the input and output impedances.

Applying the same method, the design equations of the AABH are

$$Z_1 = \frac{d_1}{d_2}\sqrt{R_a R_b}, \quad Z_2 = \sqrt{\frac{d_1^2}{d_1^2 + d_2^2}}\sqrt{R_b R_c}$$
$$Z_3 = \frac{d_1}{d_2}\sqrt{R_c R_d}, \quad Z_2 = \sqrt{\frac{d_1^2}{d_1^2 + d_2^2}}\sqrt{R_d R_a}. \tag{3}$$

A. Uniplanar Asymmetric Branch-Line Hybrid (CABH)

On the basis of the derived design equations (1) and (2), a uniplanar CABH was fabricated on Al_2O_3 substrate ($\varepsilon_r = 9.9$ and $h = 635\ \mu$m)

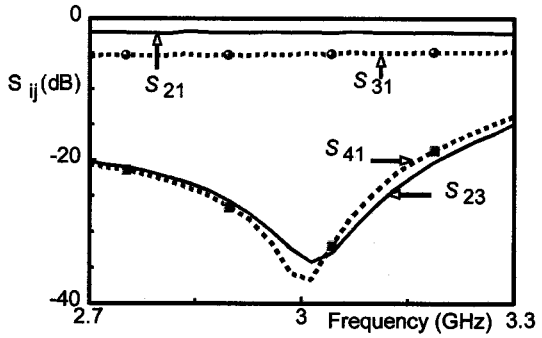

(a)

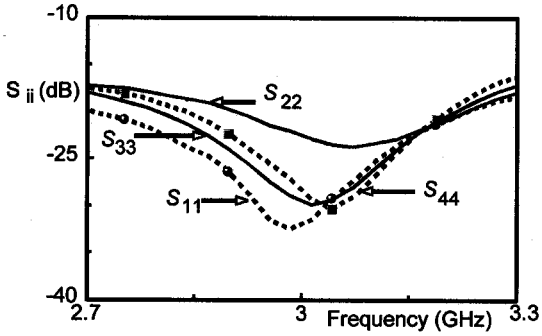

(b)

Fig. 4. Measured results of CABH terminated by 30 Ω, 60 Ω, 40 Ω and 50 Ω with a power split ratio 3 dB. (a) Power division and isolations. (b) Reflected coefficients at all ports.

using coplanar waveguide technology. This uniplanar CABH was designed with a power split ratio of 3 dB and terminated by 30 Ω, 60 Ω, 40 Ω, and 50 Ω. The experimental data of the CABH are given in Table I and Z_{01}, Z_{02}, Z_{03} and Z_{04} in Table I are the transformer-line impedances to transform termination impedances to 50 Ω. The layout of the CABH is given in Fig. 3 and all the characteristic impedances of the transmission lines are different from each other, as seen in Fig. 3. Measured power division and isolation results of the CABH are depicted in Fig. 4(a), and measured all-port matching results are plotted in Fig. 4(b). If this uniplanar CABH is ideally designed, the value of $|S_{21}|$ is -1.764 dB at the center frequency of 3 GHz from the calculation of $10\,\mathrm{Log}\lfloor d_1^2/(d_1^2 + d_2^2)\rfloor$, but the measured value of $|S_{21}|$ is -1.9259 dB. The difference between ideal and measured results comes from the losses of transmission lines, dielectric material, connectors, and so on. Since the uniplanar CABH was designed with the 3-dB power-split ratio, the ideal value of $|S_{31}|$ is -4.764 dB and the measured result of $|S_{31}|$ is -4.957 dB. From the measured results of Fig. 4(a) and (b), measured isolation results are $|S_{41}| = -34.22$ dB and $|S_{23}| = -36.62$ dB, and matchings at all ports are $|S_{11}| = -31.53$ dB, $|S_{22}| = -22.90$ dB, $|S_{33}| = -29.92$ dB and $|S_{44}| = -29.26$ dB at the center frequency of 3 GHz.

III. CONCLUSION

In this paper, asymmetric four-port hybrids, asymmetric ring hybrids, and two types of asymmetric branch-line hybrids, CABH and AABH, are newly defined depending on which port is isolated. From the definition, new design equations for the CABH and the AABH are derived. Using these components and their design equations, the size of microwave integrated circuit can be reduced.

REFERENCES

[1] W. A. Tyrrel, "Hybrid circuits for microwaves," *Proc. IEEE*, vol. 35, pp. 1294–1306, Nov. 1947.

[2] E. M. T. Jones and J. T. Bolljahn, "Coupled-strip transmission-line filters and directional couplers," *IEEE Trans. Microwave Theory Tech.*, vol. MTT-4, pp. 75–81, Apr. 1956.

[3] C. Y. Pon, "Hybrid-ring directional coupler for arbitrary power divisions," *IEEE Trans. Microwave Theory Tech.*, vol. MTT-9, pp. 529–535, Nov. 1961.

[4] S. March, "Wideband stripline hybrid ring," *IEEE Trans. Microwave Theory Tech.*, vol. MTT-16, pp. 361–362, Jun. 1968.

[5] D. Kim and Y. Natio, "Broadband design of improved hybrid-ring 3-dB directional coupler," *IEEE Trans. Microwave Theory Tech.*, vol. MTT-30, pp. 2040–2046, Nov. 1982.

[6] A. K. Agrawal and G. F. Mikucki, "A printed circuit hybrid ring directional coupler for arbitrary power division," *IEEE Trans. Microwave Theory Tech.*, vol. MTT-34, pp. 1401–1407, Dec. 1986.

[7] T. Hirota, Y. Tarusawa, and H. Ogawa, "Uniplanar MMIC hybrids—a proposed new MMIC structure," *IEEE Trans. Microwave Theory Tech.*, vol. MTT-35, pp. 576–581, June 1987.

[8] G. F. Mikucki and A. K. Agrawal, "A broadband printed circuit hybrid ring power divider," *IEEE Trans. Microwave Theory Tech.*, vol. 37, pp. 112–117, Jan. 1989.

[9] C.-H. Ho, L. Fan, and K. Chang, "Broadband uniplanar hybrid-ring and branch-line couplers," *IEEE Trans. Microwave Theory Tech.*, vol. 41, pp. 2116–2124, Dec. 1993.

[10] B.-H. Murgulescu, E. Moisan, P. Legaud, E. Penard, and I. Zaquine, "New wideband 0.67-λg circumference 180° hybrid-ring coupler," *Electron. Lett.*, vol. 30, no. 4, pp. 299–300, Feb. 1994.

[11] C.-H. Ho, L. Fan, and K. Chang, "New uniplanar coplanar waveguide hybrid-ring couplers and magic-T's," *IEEE Trans. Microwave Theory Tech.*, vol. 42, pp. 2440–2448, Dec. 1994.

[12] L. Fan, C.-H. Ho, S. Kanamaluru, and K. Chang, "Wideband reduced sized uniplanar magic-T, hybrid-ring, and de Ronde' CPW-slot couplers," *IEEE Trans. Microwave Theory Tech.*, vol. 43, pp. 2749–2758, Dec. 1995.

[13] W. W. Mumford, "Directional couplers," *Proc. IEEE*, vol. 35, pp. 159–165, Feb. 1947.

[14] R. Levy, "Analysis of practical branch-guide directional couplers," *IEEE Trans. Microwave Theory Tech.*, vol. MTT-17, pp. 289–290, May 1969.

[15] J. Reed, "The multiple branch waveguide coupler," *IEEE Trans. Microwave Theory Tech.*, vol. MTT-6, pp. 398–403, Oct. 1958.

[16] E. G. Cristal, "Coupled-transmission-line directional couplers with coupled lines of unequal characteristic impedances," *IEEE Trans. Microwave Theory Tech.*, vol. MTT-14, pp. 337–346, July 1966.

[17] R. Levy and L. F. Lind, "Synthesis of symmetrical branch-guide directional couplers," *IEEE Trans. Microwave Theory Tech.*, vol. MTT-4, pp. 80–89, Feb. 1968.

[18] L. F. Lind, "Synthesis of asymmetrical branch-guided directional coupler-impedance transformers," *IEEE Trans. Microwave Theory Tech.*, vol. MTT-17, pp. 45–48, Jan. 1969.

[19] R. K. Gupta, S. E. Anderson, and W. Getsinger, "Impedance-transforming 3-dB hybrids," *IEEE Trans. Microwave Theory Tech.*, vol. MTT-35, pp. 1303–1307, Dec. 1987.

[20] S. Kumar, C. Tannous, and T. Danshin, "A multisection broadband impedance transforming branch-line hybrid," *IEEE Trans. Microwave Theory Tech.*, vol. 43, pp. 2517–2523, Nov. 1995.

[21] J. Reed and G. J. Wheeler, "A method of analysis of symmetrical four-port networks," *IEEE Trans. Microwave Theory Tech.*, vol. MTT-4, pp. 346–352, Oct. 1956.

[22] H.-R. Ahn, I. Wolff, and I.-S. Chang, "Arbitrary termination impedances, arbitrary power division and small-sized ring hybrids," *IEEE Trans. Microwave Theory Tech.*, vol. 45, pp. 2241–2247, Dec. 1997.

[23] H.-R. Ahn, I.-S. Chang, and S.-W. Yun, "Miniaturized 3-dB ring hybrid terminated by arbitrary impedances," *IEEE Trans. Microwave Theory Tech.*, vol. 42, pp. 2216–2221, Dec. 1994.

[24] H.-R. Ahn and I. Wolff, "3-dB branch-line hybrid terminated by arbitrary impedances," *Electron. Lett.*, vol. 34, no. 11, pp. 1109–1110, May 1998.

[25] ——, "Three-port 3-dB power divider terminated by different impedances and its application to MMIC," *IEEE Trans. Microwave Theory Tech.*, vol. 47, pp. 786–794, June 1999.

[26] ——, "Three-port 3-dB power divider terminated by arbitrary impedances," in *IEEE MTT-S Dig.*, 1998, pp. 781–784.

[27] R. G. Brown, R. A. Sharpe, W. L. Hughes, and R. E. Post, *Lines, Waves, and Antennas*. New York, NY: Wiley, 1973, pp. 124–128.

[28] J. A. G. Malherbe, *Microwave Transmission Line Couplers*. Norwood, MA: Artech, 1988, p. 23.

Noise Temperature of a Lossy Flat-Plate Reflector for the Elliptically Polarized Wave-Case

T. Y. Otoshi and C. Yeh

***Abstract*—This short paper presents the derivation of equations necessary to calculate noise temperature of a lossy flat-plate reflector. Reflector losses can be due to metallic surface resistivity and multilayer dielectric sheets, including thin layers of plating, paint, and primer on the reflector surface. The incident wave is elliptically polarized, which is general enough to include linear and circular polarizations as well. The derivations show that the noise temperature for the circularly polarized incident wave case is simply the average of those for perpendicular and parallel polarizations.**

***Index Terms*—Elliptical polarization, noise temperature, point, primer, reflector.**

I. INTRODUCTION

Although equations for power in an incident and reflected elliptically polarized wave can be derived in a straightforward manner, the equations for the associated noise temperatures are not well known nor, to the authors' knowledge, can they be found in published literature. It is especially of interest to know what the relations are when expressed in terms of perpendicular and parallel polarizations and the corresponding reflection coefficients. The following presents the derivations of noise-temperature equations for three cases of interest.

II. THEORY

A. Power Relationships

For the coordinate system geometry shown in Fig. 1, the fields for an incident elliptically polarized plane wave at the reflection point are [1], [2]

$$\overline{E}_i = E_{xi}\hat{\boldsymbol{a}}_{xi} + E_{yi}\hat{\boldsymbol{a}}_{yi} \tag{1}$$

$$\overline{H}_i = H_{xi}\hat{\boldsymbol{a}}_{xi} + H_{yi}\hat{\boldsymbol{a}}_{yi} \tag{2}$$

where

$$E_{xi} = E_1 e^{j(\omega t - kz_i)} \tag{3}$$

$$E_{yi} = E_2 e^{j(\omega t - kz_i + \delta)} \tag{4}$$

$$H_{xi} = -\frac{E_{yi}}{\eta} \tag{5}$$

$$H_{yi} = \frac{E_{xi}}{\eta} \tag{6}$$

Manuscript received December 16, 1999. This work was carried out by the Jet Propulsion Laboratory, California Institute of Technology, under a contract with the National Aeronautics and Space Administration.

The authors are with the Jet Propulsion Laboratory (JPL), California Institute of Technology, Pasadena, CA 91109 USA.

Publisher Item Identifier S 0018-9480(00)07404-4.

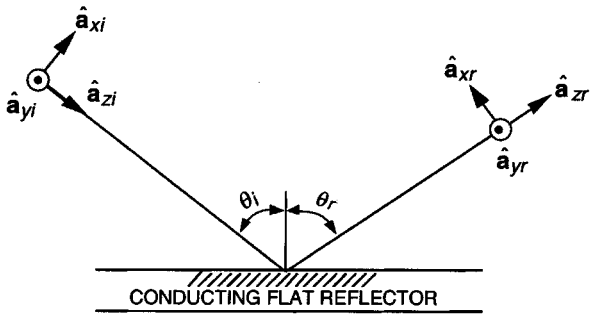

Fig. 1. Coordinate system for incident and reflected plane waves. The symbols with boldface $\hat{\boldsymbol{a}}$ are unit vectors and θ_i and θ_r are angles of incidence and reflection, respectively. The plane of incidence is the plane of this page.

where ω is the angular frequency, t is time, η is the characteristic impedance of free space, k is the free-space wavenumber, and z_i is the distance from an arbitrarily chosen source point on the incident wave ray path to the reflection point on the reflector surface (Fig. 1). In (3) and (4), it is important to note that E_1 and $E_2$are scalar magnitudes and δ is the phase difference between E_{xi} and E_{yi}.

The Poynting vector [1] for the incident wave is expressed as

$$\overline{P}_i = \frac{1}{2}\mathrm{Re}\left(\overline{E}_i \times \overline{H}_i^*\right) \tag{7}$$

where $\times$, $*$, and Re denote cross product, complex conjugate, and real part, respectively.

Then assuming all of the incident power travels through an area A in the direction of Poynting vector, the total incident wave power is

$$P_{Ti} = \int \left(\overline{P}_i \cdot \hat{\boldsymbol{a}}_{zi}\right) dA \tag{8}$$

where $\cdot$ denotes the dot product. Substitutions of (1)–(7) into (8) result in

$$P_{Ti} = \frac{1}{2\eta}\left(E_1^2 + E_2^2\right) A. \tag{9}$$

The equations for the reflected wave are obtained by replacing the subscript i with r in all of the equations for the incident wave except for (3) and (4). From Fig. 1, it can be seen that the expressions for E_{xr} and E_{yr} are

$$E_{xr} = \Gamma_{\|} E_{xi} e^{-jkz_r} \tag{10}$$

$$E_{yr} = \Gamma_{\perp} E_{yi} e^{-jkz_r} \tag{11}$$

where

$\Gamma_{\|}$ is the voltage reflection coefficient for parallel polarization at the reflection point and is a function of incidence angle θ_i (see Fig. 1)

$\Gamma_{\perp}$ is the voltage reflection coefficient for perpendicular polarization at the reflection point and is a function of incidence angle θ_i

and z_r is the distance from the reflection point on the reflector surface to an arbitrary observation point along the reflected ray path.

Then following steps similar to those used to obtain (9), the total power for the reflected wave, can be derived as

$$P_{Tr} = \frac{1}{2\eta}\left[\left|\Gamma_{\|}\right|^2 E_1^2 + \left|\Gamma_{\perp}\right|^2 E_2^2\right] A. \tag{12}$$

It is assumed that the lossy flat-plate reflector in Fig. 1 has sufficient thickness so that no power is transmitted out the bottom side. Then the dissipated power is

$$P_d = P_{Ti} - P_{Tr}. \tag{13}$$

B. Noise-Temperature Relationships

For the geometry of Fig. 1, the equation for the noise temperature of the lossy flat-plate reflector can be derived from

$$T_n = \left(\frac{P_d}{P_{Ti}}\right) T_p \tag{14}$$

where T_p is the physical temperature of the reflector in units of kelvin. For example, if the lossy conductor is at a physical temperature of 20°C, then $T_p = 293.16$K. Use of (9), (12), and (13) in (14) gives

$$T_n = \left(1 - \left|\Gamma_{ep}\right|^2\right) T_p \tag{15}$$

where

$$\left|\Gamma_{ep}\right|^2 = \frac{\left|\Gamma_{\|}\right|^2 E_1^2 + \left|\Gamma_{\perp}\right|^2 E_2^2}{E_1^2 + E_2^2}. \tag{16}$$

Equation (15) is the elliptically polarized wave noise-temperature equation that is general enough to apply to linear and circular polarizations as well. In the following, the noise-temperature expressions for three different polarization cases are derived.

Case 1: If the incident wave is linearly polarized with the E-field perpendicular to the plane of incidence, then $E_1 = 0$ and (15) becomes

$$T_n = (T_n)_{\perp} = \left(1 - \left|\Gamma_{\perp}\right|^2\right) T_p. \tag{17}$$

Case 2: If the incident wave is linearly polarized with the E-field parallel to the plane of incidence, then $E_2 = 0$ and (15) becomes

$$T_n = (T_n)_{\|} = \left(1 - \left|\Gamma_{\|}\right|^2\right) T_p. \tag{18}$$

Case 3: If the incident wave is circularly polarized, then $E_1 = E_2$ and

$$T_n = (T_n)_{cp} = \left[1 - \frac{\left(\left|\Gamma_{\|}\right|^2 + \left|\Gamma_{\perp}\right|^2\right)}{2}\right] T_p. \tag{19}$$

Note then that $(T_n)_{cp}$ is also just the average of $(T_n)_{\perp}$ and $(T_n)_{\|}$ or

$$(T_n)_{cp} = \tfrac{1}{2}\left[(T_n)_{\perp} + (T_n)_{\|}\right]. \tag{20}$$

The reader is reminded that, since the reflection coefficients are functions of incidence angle θ_i, the noise temperatures are also functions of θ_i as well as polarization.

C. Excess Noise-Temperature Relationships

It is of interest to see what the relationship is for excess noise temperature as well. For painted reflector noise-temperature analyses [3], it is convenient to use the term excess noise temperature (ENT). It is defined in [3] as the total noise temperature of a painted reflector minus the noise temperature of the reflector (bare metal) without paint. Mathematically, it is expressed as

$$\Delta T_n = T_{n2} - T_{n1} = \left(1 - \left|\Gamma_2\right|^2\right) T_p - \left(1 - \left|\Gamma_1\right|^2\right) T_p \tag{21}$$

where Γ_1 and Γ_2 are the input voltage reflection as seen looking at the unpainted (bare conductor) and painted reflector surfaces, respectively, and are functions of incidence angle and polarization. These reflection coefficients can be obtained through the use of multilayer equations such as those given in [4].

Then from (17)–(21) it follows that, for the perpendicular-, parallel-, and circular-polarization cases

$$\begin{aligned}(\Delta T_n)_\perp &= (T_{n2})_\perp - (T_{n1})_\perp \\ &= \left(1-|\Gamma_2|_\perp^2\right)T_p - \left(1-|\Gamma_1|_\perp^2\right)T_p \qquad (22)\\ (\Delta T_n)_\parallel &= (T_{n2})_\parallel - (T_{n1})_\parallel \\ &= \left(1-|\Gamma_2|_\parallel^2\right)T_p - \left(1-|\Gamma_1|_\parallel^2\right)T_p \qquad (23)\\ (\Delta T_n)_{cp} &= (T_{n2})_{cp} - (T_{n1})_{cp}\,. \qquad (24)\end{aligned}$$

Substitution of (20) into (24) gives

$$\begin{aligned}(\Delta T_n)_{cp} &= \frac{1}{2}\left[(T_{n2})_\perp + (T_{n2})_\parallel\right] - \frac{1}{2}\left[(T_{n1})_\perp + (T_{n1})_\parallel\right] \\ &= \frac{1}{2}\left\{\left[(T_{n2})_\perp - (T_{n1})_\perp\right] + \left[(T_{n2})_\parallel - (T_{n1})_\parallel\right]\right\}. \qquad (25)\end{aligned}$$

Substitutions of (22) and (23) into (25) give

$$(\Delta T_n)_{cp} = \frac{1}{2}\left[(\Delta T_n)_\perp + (\Delta T_n)_\parallel\right]. \qquad (26)$$

Equation (26) shows that the ENT for the circular-polarization case is simply the average of the ENTs of perpendicular and parallel polarizations. Although not shown mathematically, the ENTs are functions of incidence angle θ_i.

III. Applications

The NASA Deep Space Network (DSN) operates a network of large reflector antennas for deep-space communications. Minimizing the noise temperatures of these antennas and their associated receiving subsystems translates into maximizing the ground-received signal-to-noise ratios. A noise contributor that has not received much attention in the past is the noise-temperature contribution from the paints and primers on the antenna reflector surface. An example of the use of (17) and (18) is shown in Fig. 2. Noise temperatures at 32 GHz, due to 6061-T6 aluminum only [3], are shown as functions of incidence angle. An example of the use of (26) is shown in Fig. 3, which is a plot of excess noise temperature as a function of the paint thickness of Triangle no. 6 paint [3] and zinc chromate primer. This particular paint and primer has been used on all DSN antenna main-reflector and subreflector surfaces in the past. The input reflection coefficients of the multilayered dielectric stack consisting of paint, primer, and reflector were computed through the use of a computer program [4] furnished by the UCLA Electrical Engineering Department.

Water-film noise-temperature studies also can be made using the equations given in this short paper. For example, a configuration that was studied in [5] was a plane wave normally incident on a layer of water film terminated by an equivalent load assembly that consisted of a fiberglass dielectric layer bonded to the top surface of a lossless flat-plate reflector. Fig. 4 shows the overall input reflection coefficient (expressed as return loss) as a function of the equivalent load reflection coefficient phase angle. In practice, this phase angle is made variable by changing the dielectric layer thickness [5]. If the dielectric layer thickness is zero, the phase angle is 180°. If the return losses in Fig. 4 are converted to voltage reflection coefficient magnitudes, then for this

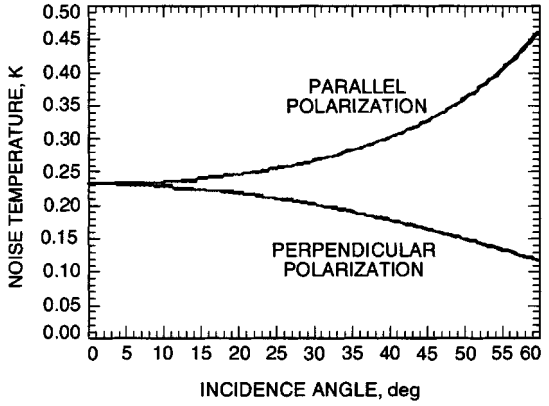

Fig. 2. The noise temperature of a flat 6061-T6 aluminum mirror at 32 GHz and 293.2K (20°C) physical temperature. Although not shown, the noise temperature curve for circular polarization is the average of those for parallel and perpendicular polarizations.

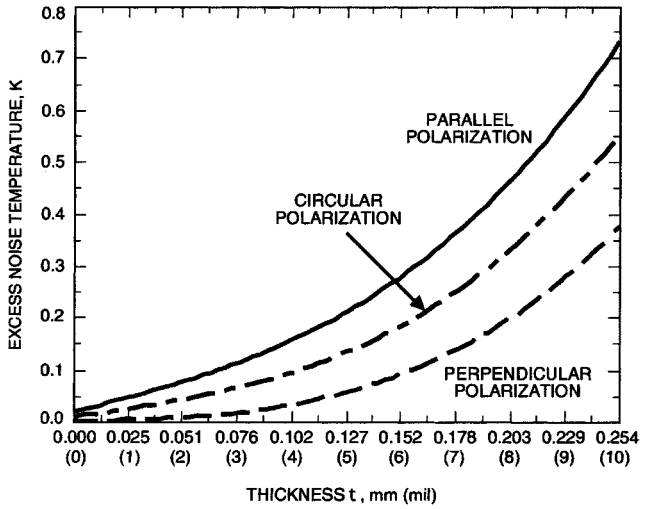

Fig. 3. The total excess noise temperature due to a Triangle no. 6 paint layer of thickness t and a fixed zinc chromate primer-layer thickness of 0.0152 mm (0.6 mil) at 30° incidence angle and 32 GHz.

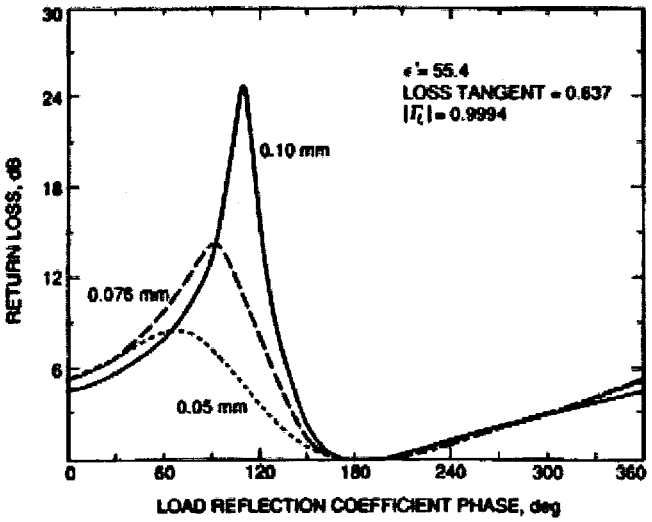

Fig. 4. Return loss versus load phase angle for various thicknesses of water films terminated in an equivalent load assembly having a reflection coefficient magnitude of 0.9994 at 12 GHz. The incidence angle for the case under study is 0°.

normal incidence case either (17) or (18) can be used to calculate the noise temperature (of the particular wet reflector configuration under study) as a function of the equivalent load reflection coefficient phase angle.

IV. Concluding Remarks

In the short paper, noise-temperature equations were derived from power equations for the incident and reflected wave. The relationships between noise temperatures of the different polarized wave cases were not obvious to the authors until the equations were derived from basic theoretical considerations. Hence, this paper serves to document the relationships and derivations. These noise-temperature formulas have proven to be useful for painted reflector studies [3] and will be useful for studies of plating [6]–[8] on reflector surfaces as well.

References

[1] S. Ramo and J. R. Whinnery, *Fields and Waves in Modern Radio*. New York: Wiley, 1953.
[2] J. A. Stratton, *Electromagnetic Theory*. New York: McGraw-Hill, 1941.
[3] T. Y. Otoshi, Y. Rhamat-Samii, R. Cirillo, and J. Sosnowski, "Noise-temperature and gain loss due to paints and primers on DSN antenna reflector surfaces," The Telecommunications and Mission Operations Progress Rep. 42-140, [Online] Available: http://tmo.jpl.nasa.gov/tmo/progress_report/42- 140/140F.pdf, Feb. 15, 2000.
[4] H.-P. Ip and Y. Rahmat-Samii, "Analysis and characterization of multi-layered reflector antennas: Rain/snow accumulation and deployable membrane," *IEEE Trans. Antennas Propagat.*, vol. 46, pp. 1593–1605, Nov. 1998.
[5] T. Y. Otoshi, "Maximum and minimum return losses from a passive two-port network terminated with a mismatched load," *IEEE Trans. Microwave Theory Tech.*, vol. 42, pp. 787–792, May 1994.
[6] E. H. Thom and T. Y. Otoshi, "Surface resistivity measurements of candidate subreflector surfaces," The Telecommunications and Data Acquisition Progress Rep. 42-65, Jet Propulsion Lab., Pasadena, CA, Oct. 15, 1981.
[7] T. Y. Otoshi and M. M. Franco, "The electrical conductivities of steel and other candidate material for shrouds in a beam-waveguide antenna system," *IEEE Trans. Instrum. Meas.*, vol. 45, pp. 73–83, Feb. 1996.
[8] ——, "Correction to 'The electrical conductivities of steel and other candidate material for shrouds in a beam-waveguide antenna system'," *IEEE Trans. Instrum. Meas.*, vol. 45, p. 839, Aug. 1996.

Multilayer Microstrip Directional Coupler with Discrete Coupling

Denis Jaisson

***Abstract*—A multilayer microstrip coupler with a high directivity has been developped, involving two strips which crossover twice at a right angle. A general full-wave model has been derived. It has been simplified in a quasi-static approximation. Based on the latter, a computer-aided design has been carried out, using finite differences in a commercial package. This design has been experimented, showing good agreement with the simplified model.**

***Index Terms*—Coupler, finite differences, microstrip, multilayer, quasi-static.**

I. Introduction

The work described in this paper was motivated by the need for a small microstrip directional coupler with an approximate 15-dB coupling factor, a directivity and a return loss at all ports greater than 20 dB within a frequency bandwidth of 5% or more around 1900 MHz. It was to serve in sampling the output signal from the power mplifier (PA) of a transmitter.

Multilayer printed circuit board (PCB) techniques that were developped for low-frequency applications are now used in microwave circuits. They involve layers of glass-epoxy FR4 or low-cost thermoset substrates developed for the mobile communications market. They give the microwave designer a new degree of flexibility in terms of the structures that can be implemented.

Taking advantage of these techniques, a novel multilayer microstrip coupler was designed, which involves two microstrip crossovers. It can be implemented at no additional cost in PCBs where other functions require multiple layers. Its geometry makes it easy to integrate, and etching tolerance is not critical.

A static electric field analysis [1] and a full-wave analysis [2] of the microstrip crossover have been reported, which were based on Green's functions. Starting with a full-wave analysis, an equivalent circuit is derived in the present paper. Modeling is simplified by making a quasi-static approximation, whereby good accuracy is maintained by accounting for both electric *and* magnetic phenomenae. In a design example, elements of the equivalent circuit are computed using a flexible finite differences (FD) method [3]. Finally, experimental results are listed.

II. The Coupler

Two kinds of couplers are used in microwave systems, which involve transmission lines in the broad sense, in order to achieve directivity. In *codirectional* couplers, incident and coupled wave travel in the same direction. These couplers can consist of two hollow metal waveguides which leak power into each other by means of *discrete* coupling through small holes machined in the wall between them [4]. These holes are $\pi/4$ apart at mid-band. There must be at least *two* of them, in order for the coupler to be directive. *Contra*directional couplers on the other hand, often involve two parallel *quasi-TEM* transmission lines such as microstrips [5], with a mixed *distributed* electric and magnetic coupling.

Manuscript received October 28, 1999.
The author is with Zydeco Developments Ltd., Ingatestone CM4 9DW, U.K. (e-mail: jaisson@usa.net).
Publisher Item Identifier S 0018-9480(00)07393-2.

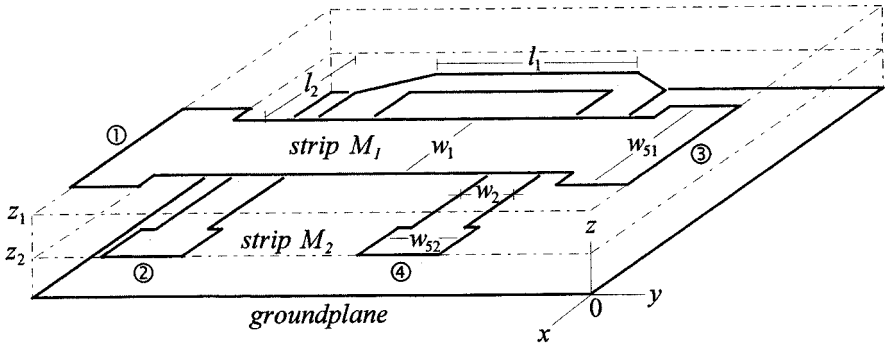

Fig. 1. Multilayer microstrip coupler.

In these couplers, incident and coupled waves travel in opposite directions.

The new structure shown in Fig. 1 is a codirectional coupler with two microstrips which couple *locally* in two places by crossing over each other. A wave that is incident at port ① of top microstrip M_1 couples to bottom microstrip M_2 through the first crossover, equally toward ports ② and ④. By the time it couples through the second crossover, phases of the first coupled signal and the incident wave have changed in such a way, that the two coupled signals cancel each other at *isolated* port ②, and add up at *coupled* port ④. The crossover in Fig. 2 was modeled, in order to combine coupled waves with proper phase and magnitude in the coupler, and achieve good directivity.

III. Full-Wave Analysis of the Crossover

In the derivation of an equivalent circuit, single-mode relationships are sought for between voltages in planes $y \equiv \pm y_1$ and $x \equiv \pm x_2$ in Fig. 2, and the currents that flow through these planes. The latter are placed at far enough a distance from the crossover, where only the fundamental mode of each microstrip can propagate. Since voltages and currents are *field integrals*, it is convenient to start from Maxwell's equations in *integral* form [6]. Losses are neglected.

Assuming thin conductors, *volume* current density $\mathbf{J}$ on M_1 and M_2 is expressed in terms of *surface* current density $\mathbf{J}_S$

$$\mathbf{J} = \mathbf{J}_S \delta(z - z_i), \qquad i = 1, 2 \tag{1}$$

where $\delta(z - z_i)$ is the pulse function of z centered on height z_i of M_i above groundplane $z \equiv 0$. The representation of $\mathbf{J}$ in (1) is adequate even at a frequency f where skin depth d_s is small compared to thickness t of M_i ($\mathbf{H} \equiv \mathbf{0}$ inside M_i) [6]. In Fig. 3, surface S_H with oriented contour C_H is wrapped around M_1 between $y \equiv \pm y_1$. $\mathbf{J}$ is related to electric and magnetic phasors $\mathbf{E}$ and $\mathbf{H}$ by

$$\oint_{C_H} \mathbf{H} \cdot d\mathbf{l} = j\omega \iint_{S_H} \varepsilon \mathbf{E} \cdot d\mathbf{S} + \iint_{S_H} \mathbf{J} \cdot d\mathbf{S}. \tag{2}$$

Bring S_H close to M_1, and join the edges of S_H which are parallel to $\mathbf{u}_y$. In (2), $\mathbf{J} \cdot d\mathbf{S} \equiv 0$. The outward flux of $\varepsilon \mathbf{E}$ through S_H is the electric charge Q_1 on M_1 between $y \equiv \pm y_1$. The contour integral of $\mathbf{H}$ is

$$\oint_{C_H} \mathbf{H} \cdot d\mathbf{l} = \int_{-w_1/2}^{+w_1/2} (\mathbf{H}(-y_1, z_1^+) - \mathbf{H}(-y_1, z_1^-)) \cdot \mathbf{u}_x \, dx$$

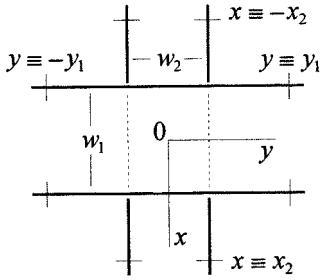

Fig. 2. Top view of the crossover.

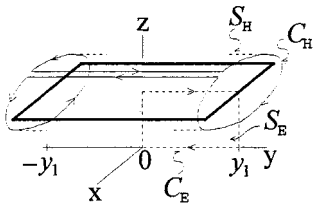

Fig. 3. Section of microstrip.

$$- \int_{-w_1/2}^{+w_1/2} (\mathbf{H}(y_1, z_1^+) - \mathbf{H}(y_1, z_1^-)) \cdot \mathbf{u}_x \, dx. \tag{3}$$

Scalar product of boundary condition

$$\mathbf{u}_z \times (\mathbf{H}(z_1^+) - \mathbf{H}(z_1^-)) = \mathbf{J}_S \tag{4}$$

with unit vector $\mathbf{u}_y$, gives the jump of $\mathbf{H}$ across M_1 in (3)

$$\oint_{C_H} \mathbf{H} \cdot d\mathbf{l} = I_1^- - I_1^+ \tag{5}$$

where

$$I_1^{\pm} = \int_{-w_1/2}^{+w_1/2} \mathbf{J}_S(\pm y_1) \cdot \mathbf{u}_y \, dx \tag{6}$$

is the total $\mathbf{u}_y$-directed current on M_1 going through $y \equiv \pm y_1$. Equation (2) can now be rewritten as

$$I_1^- - I_1^+ = j\omega Q_1. \tag{7}$$

Similarly

$$I_2^- - I_2^+ = j\omega Q_2 \tag{8}$$

where

$$I_2^{\pm} = \int_{-w_2/2}^{+w_2/2} \mathbf{J}_2(\pm x_2) \cdot \mathbf{u}_x \, dy \tag{9}$$

is the $\mathbf{u}_x$-directed current on M_2 going through $x \equiv \pm x_2$. Q_2 is the electric charge on M_2 between $x \equiv \pm x_2$.

As quantities that are *independant* of each other, the Q_i's can be expressed in terms of *any* two independant variables V_{10} and V_{20}

$$Q_i = \sum_{j=1}^{2} C_{ij}(\omega) V_{j0}, \quad i = 1, 2 \tag{10}$$

Let V_{i0} be the voltage to ground of M_i above point O

$$V_{i0} = -\int_0^{z_i} E_z(x = y = 0)\, dz. \tag{11}$$

Substituting Q_i from (10), in (7) and (8) yields

$$I_i^- - I_i^+ = \sum_{j=1}^{2} j\omega C_{ij}(\omega) V_{j0} \tag{12}$$

where $C_{12} = C_{21}$ from reciprocity [6].

Two more relationships are needed between the $I_i^{\pm}$'s and the V_{i0}'s, for the crossover to be fully characterized. Let S_E be a surface in plane $x \equiv 0$, with $0 \le y \le y_1$ and $0 \le z \le z_1$, supported by oriented contour C_E.

Using the voltage of M_1 in $y \equiv y_1$

$$V_1^+ = -\int_0^{z_1} E_z(x = 0, y = y_1)\, dz. \tag{13}$$

Maxwell integral equation

$$-\oint_{C_E} \mathbf{E} \cdot d\mathbf{l} = j\omega \iint_{S_E} \mathbf{H} \cdot d\mathbf{S} \tag{14}$$

is rewritten as

$$V_{10} - V_1^+ = -j\omega \iint_{S_E} H_x \, dy \, dz = j\omega\phi_1^+ \tag{15}$$

where ϕ_1^+ is the magnetic flux through S_E. Replacing $+y_1$ with $-y_1$ in Fig. 3 and in (13) and (15) yields

$$V_{10} - V_1^- = -j\omega\phi_1^-. \tag{16}$$

Similarly

$$V_{20} - V_2^{\pm} = \pm j\omega\phi_2^{\pm} \tag{17}$$

where

$$V_2^{\pm} = -\int_0^{z_2} E_z(x = \pm x_2, y = 0)\, dz \tag{18}$$

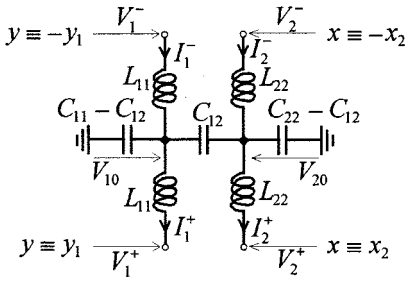

Fig. 4. Equivalent circuit of the crossover.

is the voltage of M_2 in plane $x \equiv \pm x_2$, and $\phi_2^{\pm}$ is the magnetic flux through a surface in plane $y \equiv 0$ bound by planes $x \equiv 0, \pm x_2$ and $z \equiv 0, z_2$. As independant quantities, the $\phi_i^{\pm}$'s can be expressed in terms of independant variables $I_1^{\pm}$ and $I_2^{\pm}$

$$\phi_i^{\pm} = \sum_{j=1}^{2} L_{ij}(\omega) I_i^{\pm}, \qquad i = 1, 2. \tag{19}$$

From symmetry, and because M_1 and M_2 form a right angle, currents on M_1 for example, including the relatively small transversal component, do not contribute to $\phi_2^{\pm}$.

Therefore

$$L_{12} = L_{21} = 0. \tag{20}$$

Substituting (19) and (20) into (15)–(17) yields

$$V_{i0} - V_i^{\pm} = \pm j\omega L_{ii}(\omega). \tag{21}$$

The equivalent circuit in Fig. 4 is drawn, based on (12) and (21). Because it is a *full-wave* model, **E** and **H** must be solved *simultaneously*, in order to obtain exact values for $C_{ij}(\omega)$ and $L_{ii}(\omega)$. Computation of the latter is simplified by making a quasi-static approximation, as is commonly done for single transmission lines, allowing for **E** and **H** to be treated *separately*. A model based on a static *electric* field analysis has been reported [1]. While adequate in the static case, it does not account for crossover's influence on incident **H** at f if $d_s \ll t$. M_2 for example, cannot cross under M_1 without disturbing **H** generated by M_1, and yet fulfil the boundary condition (**H** tangential to M_2), even in the case $I_2^{\pm} = 0$.

IV. Quasi-Static Approximation for the Crossover

Cut off the ends of the M_i's beyond planes $y \equiv \pm y_1$ and $x \equiv \pm x_2$, and let the latter be magnetic walls (MWs). Submit each M_i to a DC voltage V_{i0}. The behavior of the crossover is fully described by (10), where $C_{ij}(0)$ are the capacitive factors of the M_i's. Let now $y \equiv \pm y_1$ and $x \equiv \pm x_2$ be electric walls (EWs), and let each M_i carry DC current $I_i^+ = I_i^-$. The behavior of the crossover is governed by (19), where $L_{ii}(0)$ is the self-inductance of M_i. The quasi-static approximation states that

$$\begin{cases} C_{ij}(\omega) \cong C_{ij}(0) \\ L_{ii}(\omega) \cong L_{ii}(0) \end{cases} \tag{22}$$

where $C_{ij}(0)$ and $L_{ii}(0)$ are derived from *static* fields **E** and **H**. Its advantage lies in that $C_{ij}(0)$ and $L_{ii}(0)$ are computed *separately*, because *static* fields are *independant* of each other. It is stressed that $C_{ij}(\omega \neq 0)$ and $L_{ii}(\omega \neq 0)$, as defined by (10) and (19), are not capacitances and inductances proper. Indeed capacitances and inductances in general are static quantities *stricto sensu*.

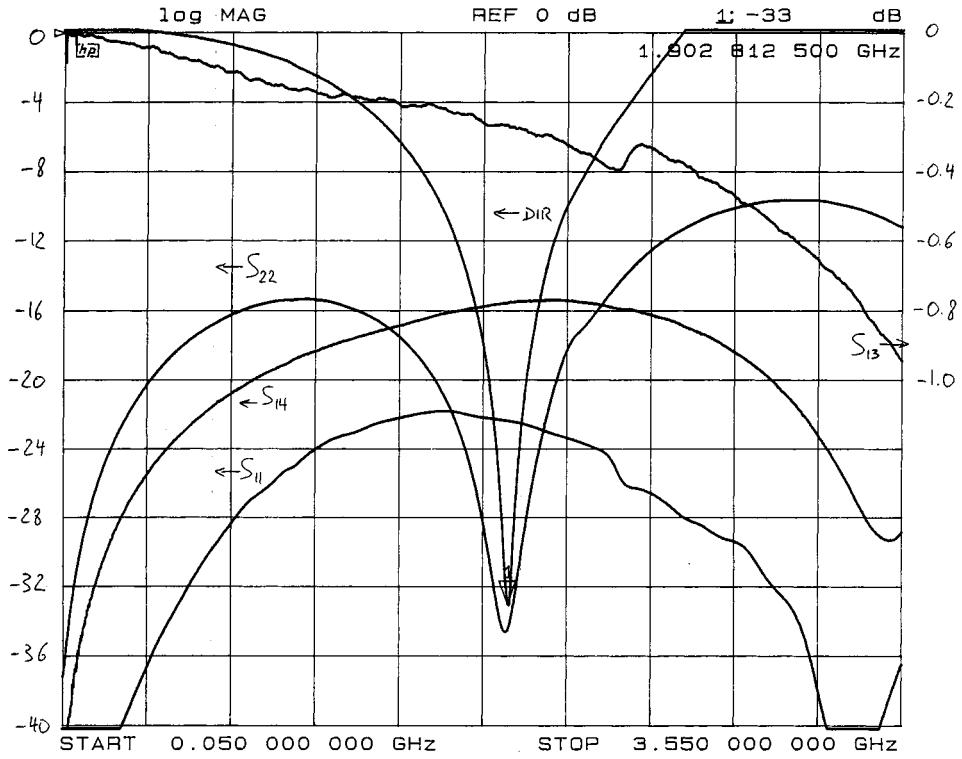

Fig. 5. Measurements of the multilayer coupler.

V. Finite Differences

$C_{ij}(0)$ and $L_{ii}(0)$ are computed using 3D*Sim*,[1] a program based on an FD method. 3D*Sim* was Zydeco's internal development program for a low-cost electromagnetic simulator. The FD method offers convenient flexibility with regard to geometry. It also allows to account for nonzero t. It is briefly outlined in this section.

In the case of C_{ij} Laplace's equation

$$\nabla^2 V = 0 \tag{23}$$

is solved for potential $\Phi = -\nabla \mathbf{E}$ in volume

$$V_{\rm FD} \begin{cases} |x| \le x_2 \\ |y| \le y_1 \\ 0 \le z \le 5z_1 \end{cases}$$

(see Fig. 2). $V_{\rm FD}$ is discretized into small boxes and $\mathbf{E}$ is approximated to a constant. At any given box corner P_i with potential Φ_i one has

$$\sum_{j=1}^{6} \Phi_j c_{ij} - \Phi_i \sum_{j=1}^{6} c_{ij} = 0, \qquad i = 1, 2, \ldots \tag{24}$$

where corner P_j is next to P_i on one of axis x, y, z.

If P_iP_j is say $\mathbf{u}_x$-directed, coefficient c_{ij} is given by

$$c_{ij} = \frac{1}{4\Delta x_{ij}} \sum_{k=1}^{4} \varepsilon_0 \varepsilon_r^{(k)} \Delta y_k \Delta z_k = \sum_{k=1}^{4} c_{ijk} \tag{25}$$

[1]3D*Sim* is a trademark of Zydeco Developments Limited. [Oline.] Available: http://www.zydeco.20m.com

where Δx_{ij} is the length of P_iP_j, Δy_k and Δz_k are the y- and z-dimensions of boxes $k = 1 \cdots 4$ which share edge P_iP_j, and $\varepsilon_r^{(k)}$ is relative permittivity inside box k. To compute C_{11} for example, boundary conditions $\Phi_{\equiv} V_1^{\pm} = 1, \Phi_{\equiv} V_2^{\pm} = 0$ and $\Phi_{\equiv} 0$ are enforced on M_1, M_2 and groundplane $z \equiv 0$, respectively. Equation (24) is a linear system with a sparse matrix. It is processed with an iterative solver [7] improved with a convergence acceleration scheme [8]. Once the Φ_i's have been computed, total capacitance $C = C_{11}$ is obtained from stored electrostatic energy

$$W = \frac{C(V_1^{\pm})^2}{2} = \frac{1}{2} \sum_i \sum_k c_{ijk} (\Phi_i - \Phi_j)^2 \tag{26}$$

C_{22} is computed for $V_{10} = 0$ and $V_{20} = 1$, and C_{12} from $C = C_{11} + C_{22} - 2C_{12}$ for $V_{10} = V_{20} = 1$. The above expression for W is *stationary* [9]. In other words, a *first*-order numerical error on Φ_i brings about a *second*-order error on C. Symmetry of the crossover about MWs $x \equiv 0$ and $y \equiv 0$ can be taken advantage of, by discretising one quarter only of $V_{\rm FD}$, and multiplying W by four.

Finding L_{ii} by solving the *electric dual* of the magnetic problem, has been suggested in the early days of discontinuity modeling for sandwiched striplines [10], whereby EWs and MWs are interchanged, and $\varepsilon_0 \varepsilon_r^{(k)}$ is replaced with μ_0 in (25). Similar to $\mathbf{E}$, field $\mathbf{H}$ of the original problem can be derived from a potential, as long as field lines do not make a closed loop around a conductor *within* $V_{\rm FD}$ [11]. This is the case when the aforementioned symmetry is used. If $I_1 = 1$ and $I_2 = 0$ for instance, MWs $\begin{cases} x \equiv 0 \\ 0 < z < z_1 \end{cases}$ and $\begin{cases} x \equiv 0 \\ z > z_1 \end{cases}$ become two EWs in the dual problem, with respective potential 0 and 1. In this case, (26) yields $C = L_{11}$. Conductors on the other hand become MWs, showing the implication of $d_s \ll t$ at f : $\mathbf{H} \equiv \mathbf{0}$ inside M_2, which may not be disregarded when L_{11} is computed.

VI. Buried Microstrip

Most commercial CAD packages for microwave circuit design do not include a model for buried microstrip M_2. The latter can be simulated using the same FD method. However, if one observes that most of the energy propagated by M_2 is located within a region where permittivity is *homogeneous* $(0 \leq z \leq z_1)$, one can save time by adapting an *existing* model for M_2, including its two bends. As has been shown and verified experimentally, M_2 can be modeled with good accuracy using the same strip with no substrates and with all dimension scaled up by factor $\sqrt{\varepsilon_r}$, connected between two ideal transformers with a $1{:}\varepsilon_r^{1/4}$ ratio [12].

VII. Design and Experiment

The coupler in Fig. 1 was designed to monitor the output power of a transmitter's PA. Because the current from the active device of this PA's last stage is large, and the output matching network requires manual trimming, top strip M_1 is connected between the PA and the transmitters antenna, while M_2 samples PA's output. Moreover losses along M_1, and therefore its length l_1, must be minimized. In a coupler with discrete coupling between two hollow waveguides, each of the latter runs over the same distance between two coupling holes. In the structure in Fig. 1, on the other hand, this distance can be given values that differ between M_1 and M_2, so as to minimize l_1, and to flatten coupling $|S_{41}|$ versus frequency somewhat.

Two substrate layers with relative permittivity $\varepsilon_r = 3.25$, height $z_2 = z_1 - z_2 = 0.787$ mm, and copper clads with $t = 18$ μm ($d_s = 1.5$ μm at 1900 MHz) were imposed. 50Ω access microstrips were kept at a $0.6\,\text{mm} = 2h$ distance from the crossovers. Their widths are, respectively, $w_{51} = 3.72$ mm for the top layer and $w_{52} = 1.51$ mm for the bottom layer. Crossovers were simulated in volume V_{FD} with $x_2 = 3w_1/2$ and $y_1 = 3w_2/2$ (Fig. 2). V_{FD} was discretized into $44 \times 49 \times 61$ boxes. 3D*Sim* gave $C_{11} - C_{12} = 0.0548$ pF, $C_{22} - C_{12} = 0.472$ pF, $C_{12} = 0.454$ pF, $L_{11} = 0.972$ nH, and $L_{22} = 1.03$ nH for just overlaping area $|x| \leq w_1/2, |y| \leq w_2/2$. These values account for proper deembedding, whereby $2w_2 \cdot C_{u1}$ and $2w_2 \cdot L_{u1}$ have been substracted, respectively, from C_{11} and L_{11} for example (C_{u1} and L_{u1} are the unit length capacitance and inductance of M_1). Touchstone predicted a 20-dB minimum directivity $|S_{41}|/|S_{21}|$ over bandwidth $B_c = 10\%$ at center frequency $f_c = 1923$ MHz, with a coupling factor $|S_{41}| = -14.3$ dB at f_c, and an $|S_{41}|$ ripple of less than 0.7 dB over B_c, for $w_1 = 3.1$ mm, $w_2 = 2.08$ mm, $l_1 = 8.73$ mm, and $l_2 = 9.43$ mm (Fig. 1).

Measurements are shown in Fig. 5. Directivity reaches a 33-dB maximum at $f_m = 1903$ MHz (keep in mind that good directivity is only useful as long as access ports are well matched). f_c is off f_m by 1% of f_m. Measured bandwidth is $B_m = 8\%$. $|S_{41}|$ goes from -15.7 to -15.4 dB over B_m, and return loss is better than 22 dB at all ports. Direct transmission loss $/|S_{31}|$ is less than 0.3 dB at f_m.

VIII. Conclusion

A new microstrip coupler was presented. It involves multiple layers which are now standard in mass production of microwave circuits for mobile communications. Good agreement between measurement and simulation was obtained, by applying an FD method to a simple quasi-static model. Measured performance show good potential for narrow-band applications, namely superior directivity. The new coupler may be the preferred choice from a manufacturing point of view also, if one considers the drawbacks of side coupling: 1) critical etching tolerance and 2) depending of the manufacturing process, dendrites might form through electrochemical migration between conductors during operation, and cause temporary shorts, especially at high power levels. This phenomenon has been identified as one of the toughest challenges of PCB bass production [13].

References

[1] S. Papatheodorou, R. F. Harrington, and J. R. Mautz, "The equivalent circuit of a microstrip crossover in a dielectric substrate," *IEEE Trans. Microwave Theory Tech.*, vol. 38, pp. 135–140, Feb. 1990.

[2] S. Papatheodorou, J. R. Mautz, and R. F. Harrington, "Full-wave analysis of a microstrip crossover," *IEEE Trans. Microwave Theory Tech.*, vol. 38, pp. 1439–1448, Oct. 1990.

[3] R. C. Booton, *Computational Methods for Electromagnetics and Microwaves*. New York: Wiley, 1992.

[4] R. E. Collin, *Foundations for Microwave Engineering*. New York: McGraw-Hill, 1966.

[5] T. C. Edwards, *Foundations for Microstrip Circuit Design*. New York: Wiley, 1983.

[6] R. F. Harrington, *Time-Harmonic Electromagnetic Fields*. New York: McGraw-Hill, 1961.

[7] G. H. Golub and C. H. Van Loan, *Matrix Computations*. Baltimore, MD: John Hopkins Univ. Press, 1983.

[8] K. J. Binns and P. J. Lawrenson, *Analysis and Computation of Electric and Magnetic Field Problems*, Oxford, U.K.: Pergamon, 1963.

[9] R. E. Collin, *Field Theory of Guided Waves*. New York: McGraw-Hill, 1960.

[10] A. A. Oliner, "Equivalent circuits for discontinuities in balanced strip transmission lines," *IRE Trans. Microwave Theory Tech.*, vol. MTT-3, pp. 134–143, Mar. 1955.

[11] J. A. Stratton, *Electromagnetic Theory*. New York: McGraw-Hill, 1941.

[12] D. Jaisson, "Design microstrip components with a dielectric cover," in *Microwaves RF*, Feb. 1993, pp. 71–80.

[13] Concoat Ltd., "Compatibility issues in board design," *Electron. Product News*, p. 12, Mar. 2000.